Published in final edited form as:

Cell Stem Cell. 2019 December 05; 25(6): 830–845.e8. doi:10.1016/j.stem.2019.08.017.

PRDM16 maintains homeostasis of the intestinal epithelium by controlling region-specific metabolism

Rachel R. Stine[1,2,*], **Alexander P. Sakers**[1,2], **Tara TeSlaa**[3], **Megan Kissig**[1,2], **Zachary E. Stine**[4], **Chan Wook Kwon**[1,2], **Lan Cheng**[1], **Hee-Woong Lim**[5], **Klaus H. Kaestner**[1,6], **Joshua D. Rabinowitz**[3], **Patrick Seale**[1,2,7,*]

[1] -Institute for Diabetes, Obesity & Metabolism, Smilow Center for Translational Research, Perelman School of Medicine, University of Pennsylvania, Philadelphia, PA, 19104, USA

[2] -Department of Cell and Developmental Biology, Smilow Center for Translational Research, Perelman School of Medicine, University of Pennsylvania, Philadelphia, PA, 19104, USA

[3] -Lewis-Sigler Institute for Integrative Genomics and Department of Chemistry, Princeton University, Princeton, NJ, 08544, USA

[4] -Wistar Institute, Philadelphia, PA, 19104, USA

[5] -Department of Biomedical Informatics, Cincinnati Children's Hospital Medical Center, Cincinnati, OH, 45229, USA

[6] -Department of Genetics, Smilow Center for Translational Research, Perelman School of Medicine, University of Pennsylvania, Philadelphia, PA, 19104, USA

[7] -Lead contact

Summary

Metabolic pathways dynamically regulate tissue development and maintenance. However, the mechanisms that govern the metabolic adaptation of stem or progenitor cells to their local niche are poorly understood. Here, we define the transcription factor PRDM16 as a region-specific regulator of intestinal metabolism and epithelial renewal. PRDM16 is selectively expressed in the upper intestine, with enrichment in crypt-resident progenitor cells. Acute *Prdm16* deletion in mice

---

[*] Institute for Diabetes, Obesity & Metabolism, Smilow Center for Translational Research, Perelman School of Medicine, University of Pennsylvania, Philadelphia, PA, USA stiner@pennmedicine.upenn.edu, sealep@pennmedicine.upenn.edu.

Author Contributions

R.R.S. and P.S. conceived the project and wrote the manuscript, with important input from K.K. R.R.S designed, performed and interpreted the majority of the experiments A.P.S performed RNA-seq analysis and flow-sorting experiments. T.T performed and analyzed the liquid chromatography-mass spectrometry (LC-MS) tracing experiments with input from J.D.R. C.W.K. participated in enteroid experiments and characterization of mouse models. M.K. participated in glucose-tracing experiments, ChIP, and crypt isolation for RNA and Western blot analysis. H.W.L performed ChIP-seq analysis. L.C. performed histological and immunofluorescence studies. Z.E.S assisted in the conception and execution of metabolic tracing experiments, writing of manuscript and data interpretation.

Accession

All sequencing data is available at GSE121014.

Declaration of Interests: The authors declare no competing interests.

triggered progenitor apoptosis, leading to diminished epithelial differentiation and severe intestinal atrophy. Genomic and metabolic analyses showed that PRDM16 transcriptionally controls fatty acid oxidation (FAO) in crypts. Expression of this PRDM16-driven FAO program was highest in the upper small intestine and declined distally. Accordingly, deletion of *Prdm16* or inhibition of FAO selectively impaired the development and maintenance of upper intestinal enteroids, and these effects were rescued by acetate treatment. Collectively, these data reveal that regionally specified metabolic programs regulate intestinal maintenance.

Graphical Abstract

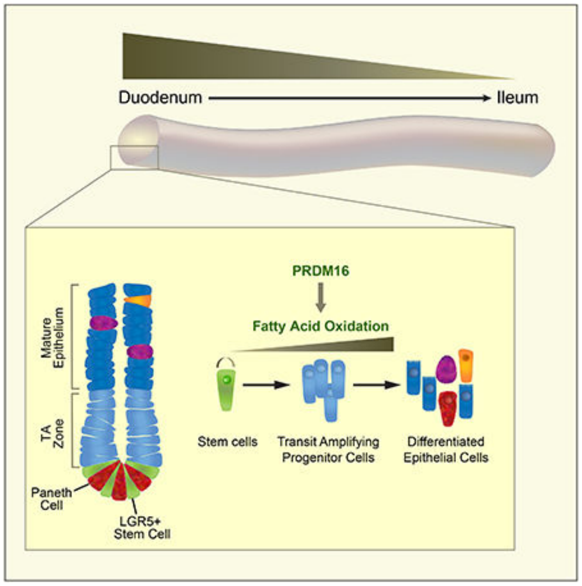

Introduction

The small intestinal epithelium is organized into repeating crypt-villus units. The villi are finger-shaped projections that are specialized for nutrient absorption. The crypt, located at the base of each villus, contains proliferative stem cells responsible for epithelium maintenance (Barker et al., 2007). Stem cells produce transit-amplifying (TA) progenitor cells that divide and migrate out of the crypt and up the villus as they differentiate into absorptive or secretory epithelial cells.

The villus epithelium undergoes rapid renewal by stem cells every few days. The constitutively high levels of intestinal stem and progenitor cell proliferation is supported by specific metabolic pathways (Folmes et al., 2012; Potten and Loeffler, 1990; Wang et al., 2018; Wei et al., 2018). In addition to providing energy and building blocks, cellular metabolism influences chromatin structure and gene expression through a variety of mechanisms (Ito and Ito, 2016). For example, nutritional status and metabolic pathway activity regulate the availability of substrates for DNA and histone modifications (Folmes et al., 2012).

Recent studies have begun to elucidate the importance of metabolism in regulating intestinal stem cells. In particular, pyruvate oxidation in stem cells drives pro-differentiation signaling (Rodriguez-Colman et al., 2017; Schell et al., 2017). Additionally, fatty acid oxidation (FAO) is required for proper stem cell function (Mihaylova et al., 2018). The metabolic behavior of intestinal stem and progenitor cells is modulated by nutritional status, including fasting and high fat diet, accompanied by changes in cell survival, rates of proliferation and tumor-forming capacity (Beyaz et al., 2016; Mihaylova et al., 2018; Wang et al., 2018). However, relatively little is known about the transcriptional pathways that specify the metabolic features of intestinal stem and progenitor cells.

PRDM16 is a transcription factor that drives high levels of oxidative metabolism and mitochondrial respiration in brown fat cells (Cohen et al., 2014; Ohno et al., 2012; Seale et al., 2008; Seale et al., 2011; Wang et al., 2019). PRDM16 enhances the transcriptional function of Peroxisome proliferator-activated receptors (PPARs), including PPARα and PPARγ, to promote metabolic gene transcription in fat cells (Seale et al., 2008). Intriguingly, PRDM16 also regulates the activity of certain stem cell populations, including hematopoietic and neural stem cells (Aguilo et al., 2011; Chuikov et al., 2010; Cohen et al., 2014; Inoue et al., 2017; Shimada et al., 2017).

Here we show that PRDM16 is essential for the maintenance of the small intestinal epithelium. PRDM16 expression is enriched in crypt-resident progenitor cells, selectively in the upper small intestine. Deletion of *Prdm16* causes apoptosis in progenitor cells and leads to a diminished production of differentiated progeny. PRDM16 regulates intestinal renewal, at least in part, by stimulating FAO. Notably, the PRDM16-driven FAO program is highest in the proximal small intestine and declines distally. The development and maintenance of enteroids generated from upper but not lower regions of the small intestine rely on PRDM16 and FAO. Together, these results demonstrate that upper intestinal renewal depends on a regionally-specified program of FAO.

Results

Prdm16 is required for small intestinal maintenance

PRDM16 controls brown fat development and regulates hematopoietic and neural stem cell activity (Aguilo et al., 2011; Chuikov et al., 2010; Seale et al., 2008). However, the role of PRDM16 in other adult tissues is largely unknown. We assessed the effects of *Prdm16* deletion in 6-week-old mice using a tamoxifen (tmx)-inducible Cre ($R26R^{Cre-ERT2}$; $Prdm16^{loxP/loxP}$). Deletion of *Prdm16* induced a rapid-onset wasting phenotype, including weight loss and diarrhea, with mutant mice dying in ~7-10 days (Fig. 1A). Necropsy revealed gross changes in the small intestine of mutant animals, which were noticeably pale, distended and filled with watery, bile colored feces (Fig. 1B). *Prdm16* mRNA was decreased by >90% and PRDM16 protein was undetectable in the duodenum by 3 days post tmx treatment (Fig. S1A–B). By day 7, the small intestines of *Prdm16*-deficient animals were approximately two-thirds the length of sibling controls (Fig. 1C). H&E staining showed that the duodenum of *Prdm16*-mutant mice contained highly disorganized columnar epithelial cells and underwent progressive villus shortening (Fig. 1D, S1C).

We assessed barrier function by gavaging animals with FITC-dextran and measuring its appearance in the serum. *Prdm16*-deficient mice had markedly increased blood FITC levels, along with increased colony forming units when whole blood was cultured (Fig. S1D,E). *Prdm16*-deficient mice also had elevated levels of blood cytokines (IL-10, TNFα, Eotaxin), associated with the onset of sepsis (Fig. S1F) (Shrum et al., 2014).

Prdm16 is highly expressed in small intestinal crypts

Analysis of *Prdm16* expression across a panel of adult mouse tissues revealed the highest expression levels in the small intestine and stomach (Fig. S1G). *PRDM16* mRNA levels were also at their highest in human duodenum and stomach (Fig. S1H) (https://www.proteinatlas.org) (Uhlen et al., 2015). Immunofluorescence staining of mouse duodenum showed that PRDM16 protein was present at higher levels in crypts relative to villi, with enrichment in TA zone cells, localized directly above *Lgr5*-GFP+ stem cells at the crypt base (Fig. 1E). This staining was lost in *Prdm16*-mutant crypts, validating the antibody specificity (Fig. S1I). Consistent with the immunostaining results, *Prdm16* mRNA levels were higher in flow-sorted *Lgr5*-GFP^{low} cells than in *Lgr5*-GFP^{high} stem cells from crypts (Fig. 1F).

Prdm16 promotes the survival and proliferation of crypt-resident progenitor cells

We next examined the effect of *Prdm16*-deletion on crypt cell fate. At 5 days post tmx, *Prdm16* mutant duodenal crypts contained reduced numbers of proliferating cells, marked by Ki67 expression (Fig. 2A). Mutant crypts also displayed a prominent increase in the number of Cleaved Caspase-3+ apoptotic cells (Fig. 2B). Most apoptotic cells were located in the TA zone and did not correspond to *Lgr5*-GFP^{high} stem cells at the crypt base (Fig. 2B). Crypts from control and mutant mice contained equivalent numbers of *Lgr5*-GFP^{high} stem cells at 5 days post tmx treatment, a time point when villus architecture is disrupted and epithelial cell number is decreased (Fig. 2C,D). Flow cytometry analysis also showed that control and *Prdm16*-mutant crypts contained similar proportions of *Lgr5*-GFP+ stem cells (Fig. S2A). Control and mutant crypts also expressed equivalent mRNA levels of *Lgr5* and *Ascl2,* markers of crypt base columnar (CBC) stem cells (Fig. 2E). By contrast, expression of the stem cell marker *Olfm4* was downregulated by *Prdm16*-deletion (Fig. 2E). Marker genes of the reserve or “+4” stem cells, *Bmi1* and *Hopx,* were upregulated in *Prdm16*-mutant crypts (Fig. 2E) (Takeda et al., 2011; Yan et al., 2012).

Prdm16-deletion skews intestinal cell type composition

Immunostaining revealed that *Prdm16* mutant crypts contained anomalous granular cells co-expressing the Paneth cell marker Lysozyme (LYZ) and the goblet cell marker Mucin 2 (MUC2) (Fig. 2F). The induction of cells co-expressing goblet and Paneth cell markers has been linked to inhibition of the Notch pathway (VanDussen et al., 2012). However, *Prdm16*-deletion did not reduce expression of the Notch intracellular domain (NICD) or canonical Notch pathway components in crypts (Fig. S2B, C).

Intestinal crypt progenitors normally migrate up the villi, giving rise to differentiated epithelium, including absorptive enterocytes and secretory cells. The *Prdm16*-mutant villi and crypts expressed higher levels of many secretory cell marker genes, including *Tff3* (goblet cells), *Mmp7* (Paneth cells) and *Reg4* (enteroendocrine cells) along with dramatically reduced levels of absorptive enterocyte markers *Sis* and *Lct* (Fig. 2G, Fig. S2D). *Prdm16*-deletion did not significantly affect expression of tuft cell markers, including *Dclk1* (Fig. 2G, S2D). Consistent with these mRNA expression changes, immunofluorescence studies showed that *Prdm16* mutant villi contained more CHGA+ enteroendocrine and MUC2+ goblet cells (Fig. S2E,F).

Stem cell-selective Prdm16 deletion reduces the development of mature epithelial cells

To further investigate the role of PRDM16 in regulating intestinal renewal, we generated a stem cell-specific *Prdm16* knockout mouse model using the $Lgr5^{GFP/CreERT2}$ ($Prdm16^{\Delta Lgr5}$) driver. This Cre driver has a mosaic expression pattern (Barker et al., 2007; Sato et al., 2009), allowing us to examine the role of PRDM16 in the turnover of intestinal epithelium without the confounding effect of whole organ failure. As anticipated, $Prdm16^{\Delta Lgr5}$ mice displayed a less severe intestinal phenotype than global mutant mice (Fig. S3A). We confirmed that PRDM16 protein expression was absent in a subset of crypts from these mice (Fig. 3A). Similar to results in the global mutant animals, *Prdm16*-deletion in *Lgr5*+ cells did not affect stem cell number and led to elevated crypt cell apoptosis and the induction of abnormal MUC2+;LYZ+ cells in crypts (Fig. 3B–D). Neither the stem cell specific nor global *Prdm16* mutant mice had significantly increased numbers of apoptotic cells in villi (Fig. S3B).

To examine the fate of control and *Prdm16*-mutant *Lgr5*+ stem cells, we integrated a Cre-inducible tdTomato reporter gene into the $Prdm16^{\Delta Lgr5}$ mice. Tmx induces Cre activity in *Lgr5*+ cells, driving heritable tdTomato expression and concurrent deletion of *Prdm16* in mutant animals. The intestines of control and *Prdm16* mutant reporter mice were analyzed 3 and 14 days after tmx treatment. At 3 days, the length of tdTomato-marked epithelial strips along the crypt-villus axis was reduced by ~30% in *Prdm16* mutant animals (~380 μM in controls compared to ~270 μM in mutant; Fig. 3E, S3C). At day 14, lineage-traced *Prdm16* mutant stem cells (tdTomato+;*Lgr5*-GFP+) were still present at the base of the crypts (Fig. 3F). Similar to the results at the earlier time point, mutant cells generated reduced numbers of differentiated epithelial progeny in villi, as evidenced by shorter strips of tdTomato+ cells (~625 μM in control vs ~400 μM in mutant; Fig. 3F).

Prdm16 is required for intestinal enteroid differentiation and maintenance

Intestinal enteroids, generated from whole crypts or *Lgr5*+ stem cells, are an established model system for studying intestinal development and maintenance (Sato et al., 2009). When cultured with growth factors that support a balance of stem cell maintenance and differentiation (EGF + R-Spondin + Noggin = ENR media), stem cells and descendent progenitor cells divide and give rise to mature epithelial cell populations, forming buds with stem cells located away from the enteroid centers.

We generated enteroids from crypts of control ($Prdm16^{loxP/loxP}$) and mutant ($R26R^{Cre\text{-}ERT2}$; $Prdm16^{loxP/loxP}$) mice in ENR medium. Once established, the enteroids were treated with 4-hydroxytamoxifen (4-OHT) to delete *Prdm16*. Control enteroids continued to grow in size and underwent extensive budding. By contrast, *Prdm16*-deletion led to the formation of small, cystic enteroids that failed to bud (Fig. 4A). ShRNA-mediated knockdown of *Prdm16* also diminished the recovery of viable enteroids (Fig. S4A).

Deletion of *Prdm16* in fully mature enteroids induced bud regression with mutant enteroids assuming a stunted and circular morphology (Fig. 4B; S4B). By contrast, control enteroids continued to grow in size and complexity, producing more and larger buds (Fig. 4B). *Prdm16*-mutant enteroids retained *Lgr5*-GFP+ stem cells during culture (Fig. 4C). As observed in mouse intestine, *Prdm16*-deletion in enteroids triggered apoptosis and decreased the expression of *Ki67,* a proliferation marker (Fig. 4D, S4C). *Prdm16*-mutant enteroids also expressed elevated levels of many secretory cell genes, including *Tff3* (goblet cells), *Mmp7* (Paneth cells) and *Reg4* (enteroendocrine cells) (Fig. 4E, S4D–G). The mRNA levels of absorptive cell markers were not decreased in *Prdm16* mutant enteroids (Fig. S4G). The expression of CBC stem cell markers *Ascl2* and *Lgr5* were decreased by ~2-fold in *Prdm16*-deleted enteroids, though these effects were not statistically significant at most time points (Fig. 4E).

Enteroids can be maintained and propagated in an undifferentiated state by adding high amounts of WNT3A to the culture medium (Wnt^{High} + EGF + Noggin + R-Spondin = WENR media) (Fig. 4F) (Rodriguez-Colman et al., 2017; Sato et al., 2009). Spheroids formed under these conditions lack buds and contain homogenously proliferating cells with elevated expression of embryonic markers (Rodriguez-Colman et al., 2017). When cultured in Wnt^{high} (WENR) conditions, *Prdm16*-deficient enteroids appeared grossly normal and grew in size at a similar rate as control enteroids (Fig. 4G, S4H). Subsequent removal of WNT3A to induce differentiation caused *Prdm16*-deficient enteroids to shrink and accumulate dark lumenal debris, while control enteroids continued to grow in size and underwent robust budding (Fig. 4H, S4H).

We tested whether PRDM16 was required for the formation of secondary enteroids, reflecting the renewal capacity of enteroid-forming (stem or progenitor) cells. *Prdm16*-deficient enteroids had no capacity to produce secondary enteroids when passaged in ENR conditions (Fig. 4I). In Wnt^{High} (WENR) conditions, *Prdm16*-deficient enteroids generated secondary enteroids, albeit at lower rates than control enteroids (Fig. 4I). We also compared the enteroid-forming capacity of control and *Prdm16* mutant stem and progenitor cells. *Lgr5*-GFP^{high} stem cells and *Lgr5*-GFP^{low} cells (*Lgr5*+ descendants) were isolated by FACS from control and *Prdm16* mutant intestines three days after tmx treatment. The sorted cells were combined with wildtype Paneth cells (CD24^{hi}, c-KIT^{hi}, GFP^{neg}) at a 1:1 ratio prior to embedding in Matrigel. *Lgr5*-GFP^{high} and *Lgr5*-GFP^{low} cells from control mice displayed robust colony forming activity (Fig. 4J). *Prdm16*-deletion reduced colony formation in GFP^{high} and GFP^{low} cells by 61% and 72%, respectively, relative to corresponding controls (Fig. 4J). At a morphological level, control stem cells formed highly budded enteroids over the course of 14 days, while mutant stem cells generated cystic colonies that failed to bud (Fig. 4J). We also quantified colony formation of *Lgr5*-GFP^{high} and *Lgr5*-GFP^{low} cells cultured in Wnt^{high} (WENR) medium. Again, *Prdm16* mutant cells generated fewer colonies than control (wildtype) cells (Fig. 4K). In particular, the colony forming activity of *Prdm16*-deficient *Lgr5*-GFP^{low} (*Lgr5*+ descendant) cells was reduced by >90%. These data demonstrate that PRDM16 regulates the renewal capacity of enteroid-forming cells.

Prdm16 deletion induces type I interferon and p53 gene signatures

To identify PRDM16-target pathways in intestinal crypts, we compared the gene expression profiles of control and *Prdm16*-mutant duodenal crypts 3 days post tmx injection. At this time point, PRDM16 protein was depleted in mutant crypts, but changes in intestinal architecture had not yet manifested (Fig. 1D, S1B). The upregulated genes in *Prdm16*-mutant vs. control crypts were highly enriched for p53 and type I interferon pathway components (Fig. S5A,B, Table S1A,B) (Porta et al., 2005). Crossing *Prdm16*-mutant mice onto a conditional *p53* mutant background prevented the P53 target gene response in crypts, but did not rescue their intestinal renewal deficit (Fig. S5C–F). Enteroids generated from *Prdm16/p53*-mutant mice displayed severe growth and maturation defects, though expression of *Olfm4* was restored back to control levels (Fig. S5G–H). Additionally, blocking type I interferon signaling and target gene expression using a neutralizing antibody did not normalize the phenotype of *Prdm16*-mutant enteroids (Fig. S5I–K). These results indicate that neither elevated p53 activity nor interferon signaling are sufficient to cause the intestinal deficits caused by *Prdm16*-deletion.

PRDM16 regulates metabolic genes/pathways in small intestinal crypts

Pathway analysis of downregulated genes in *Prdm16*-mutant vs. control crypts revealed a striking enrichment in metabolic pathways, including biological oxidation, mitochondrial fatty acid beta-oxidation, retinoic acid biosynthesis and fatty acid, triacylglycerol and ketone body degradation (Fig. 5A, Table S1C,D). In particular, *Prdm16*-mutant crypts expressed lower levels of genes involved in multiple steps of fatty acid utilization, including fatty acid uptake and acylation (*Cd36, Slc27a2, Acsl1*), acyl-carnitine mitochondrial import (*Cpt1a* and *Cpt2*), mitochondrial fatty acid oxidation (FAO; *Acadm, Acaa2, Hadh*), and mono and polyunsaturated FAO (*Eci1, Eci2, Decr1*) (Fig. 5B,C). Many of these genes were further downregulated at later time points as the mutant phenotype progressed (Fig. 5D). FAO gene levels were also reduced, albeit to a lesser extent, in mutant compared to control villi (Fig. S5L). In addition to decreasing FAO gene levels, loss of *Prdm16* reduced the expression of genes involved in the TCA cycle, amino acid catabolism and retinol metabolism (Fig. S5M).

To investigate the mechanism by which PRDM16 regulates FAO genes, we performed ChIP-seq for PRDM16 and the active enhancer mark H3K27Ac in control and *Prdm16*-deficient crypts. PRDM16 binding sites were located closer to genes whose expression was downregulated in *Prdm16*-mutants, compared to unchanged or increased genes, suggesting that PRDM16 largely functions as a transcriptional activator in crypts (Fig. 5E). Prominent PRDM16 binding sites were identified at several FAO gene loci, including *Slc27a2, Acsl1, Cpt2, Acaa2, Hadh, Decr1* and *Eci2,* with many of these sites showing decreased H3K27Ac levels in mutant vs. control crypts (Fig. 5F, S5N).

PRDM16 binding sites were enriched with motifs for several transcription factors, including PPARs, which are known to regulate FAO (Fig. 5G, Table S1E) (Ito et al., 2012). Motif analysis of regions with reduced H3K27Ac levels in mutant vs. control crypts identified a similar set of motifs (Fig. S5O, Table S1F). ChIP-qPCR analysis of intestinal crypts showed that PPARα and PPARγ bind to the same sites as PRDM16 at many FAO genes, including *Slc27a2, Cpt1a, Cpt2, Acaa2, Hadh, Decr1* and *Eci2* (Fig. 5H). Previous studies have shown that PRDM16 physically interacts with PPARα and PPARγ, and enhances their transcriptional function (Hondares et al., 2011; Seale et al., 2008). Treatment of wild type duodenal enteroids with antagonists of PPARγ and PPARα, either separately or in combination, led to severe developmental defects. Antagonism of PPARγ blocked enteroid budding and induced apoptosis, while inhibition of PPARα caused a complete loss of viability (Fig S5P,Q). Thus, these data provide evidence that PRDM16, along with PPAR proteins, directly activate the expression of FAO genes in intestinal crypts.

Prdm16 regulates FAO in small intestinal crypts

To assess the role of PRDM16 in regulating FAO, we performed stable isotope tracing in control and *Prdm16*-deficient duodenal crypts. Crypts isolated from control and mutant mice 3 days after tmx injection were incubated in medium containing uniformly labeled $^{13}C_{16}$-palmitate (Fig. 6A, S6A). We then measured ^{13}C integration into the TCA cycle intermediates citrate and α-ketoglutarate (Fig. 6B). Labeling was assessed by calculating the percentage of ^{13}C labeled carbons in each metabolite pool (Fendt et al., 2013). $^{13}C_{16}$-palmitate was efficiently incorporated into citrate and α-ketoglutarate in control crypts, with over 20 percent of carbons labeled with ^{13}C (Fig. S6B). *Prdm16* deficient crypts displayed a ~30% reduction in relative ^{13}C labeling of both citrate and α-ketoglutarate (Fig. 6B, S6B). At this time point, the expression of FAO genes had begun to decrease in *Prdm16*-deficient crypts and continued to drop over subsequent days (Fig. 5D). Of note, the FAO regulators *Ppara* and *Pparg* as well as the mitochondrial acyl-carnitine importers *Cpt1a* and *Cpt2* were expressed at higher levels in *Lgr5*-GFP^{low} (*Lgr5*+ descendant) cells compared to *Lgr5*-GFP^{High} stem cells, following the same pattern as *Prdm16* (Fig. 6C, 1F).

We also assessed glucose metabolism in control and *Prdm16*-mutant enteroids using $^{13}C_6$-glucose stable isotope tracing. *Prdm16* mutant enteroids displayed a small but significant increase in the incorporation of ^{13}C labeled carbons (from glucose) into citrate and α-ketoglutarate (Fig. S6C). This result demonstrates that loss of *Prdm16* does not disrupt general mitochondrial oxidative activity and, if anything, increases glucose utilization. While we did not observe widespread expression changes in the levels of glycolytic genes in mutant crypts, the glucose transporter *Glut1/Slc2a1* and hexokinases *Hk1* and *Hk2* were upregulated (Fig. S6D).

To determine if blocking FAO mimics the phenotypic effect of *Prdm16*-deficiency, we treated duodenal enteroids with the CPT1 inhibitor etomoxir. Etomoxir treatment of enteroids reduced their growth, budding and capacity to generate secondary enteroids (Fig. 6D–G). Acetate, by providing an alternate source of acetyl-CoA rescues genetic or etomoxir-mediated inhibition of FAO (Schug et al., 2016; Wong et al., 2017). While etomoxir has off-target effects in some tissues, these effects are not reversed by acetate (Yao et al., 2018). We found that acetate completely rescued the growth and budding defects and significantly increased secondary enteroid formation in etomoxir-treated enteroids (Fig. 6E–G). Acetate did not augment the growth, budding or passaging capacity of control enteroids.

These results led us to ask whether acetate could substitute for FAO and rescue the intestinal defects caused by *Prdm16*-deficiency. Strikingly, acetate supplementation fully rescued the altered morphology and growth deficit of *Prdm16*-deficient enteroids, while also suppressing the induction of Cleaved Caspase-3+ (apoptotic) cells (Fig. 6H, I, S6E). Acetate also prevented the increased formation of Lysozyme+ cells in *Prdm16*-deleted enteroids and normalized the expression of secretory cell marker genes (*Tff3, Mmp7, Chga*) (Fig. 6J,K). The stem cell genes *Ascl2* and *Lgr5* were moderately downregulated by acetate in control enteroids. However, acetate prevented the downregulation of these genes upon *Prdm16*-deletion (Fig. 6K). As shown above, *Prdm16*-deletion severely impaired secondary enteroid formation in ENR medium (Fig. 6L). However, in acetate-supplemented medium, control and mutant enteroids generated comparable numbers of secondary enteroids, similar to that of control (no acetate) enteroids (Fig. 6L, images in S6F). Finally, acetate significantly increased budding frequency in *Prdm16*-mutant enteroids (Fig. 6M).

We next tested if acetate could rescue the impaired development of villus epithelium by *Prdm16*-deficient stem cells *in vivo*. To do this, control and *Prdm16*-mutant *Lgr5*^{CreERT}; *R26R-tdTomato* reporter mice were given drinking water containing either 150 µM sodium acetate or 150 mM sodium chloride (as control) beginning two days before tmx injection and continuing throughout the course of the experiment. As observed before, the development of tdTomato+ villus epithelial cells was severely reduced in *Prdm16* mutant mice under control conditions (Fig. 6N). Acetate-treatment had very little effect on epithelial cell development in control mice. By contrast, acetate supplementation markedly increased the development of tdTomato+ villus epithelial cells in *Prdm16*-mutant mice, almost reaching the levels observed in controls (Fig. 6N). In line with this, acetate blocked the induction of apoptotic cells and Lysozyme+ cells and blunted the induction of Mucin2+ cells in *Prdm16*-mutant mice (Fig. 6O, S6G–I). Thus, acetate treatment rescues many of the phenotypic consequences of *Prdm16*-deficiency in intestinal stem cells and further implicates a crucial role for PRDM16-driven FAO in promoting intestinal renewal.

PRDM16 is a region-specific regulator of small intestinal metabolism and renewal

We noted that the jejunum and ileum had milder phenotypes than the duodenum in *Prdm16*-mutant mice (Fig. S7A). This led us to examine PRDM16 expression along the length of the intestine. Immunostaining of a full length, small intestinal “Swiss roll” showed high PRDM16 protein expression in the duodenum, with gradually decreasing expression toward the ileum (Fig. 7A). This PRDM16 expression pattern was confirmed by western blot analyses of crypt samples from different intestinal regions (Fig. 7B). *Prdm16* mRNA levels were also highest in duodenal crypts compared to crypts isolated from more distal regions (Fig. 7C).

To determine if PRDM16 is required in a region-specific manner, we studied the effect of *Prdm16*-deletion in enteroids established from duodenal, jejunal and ileal crypts. The cultured enteroids expressed region-selective signature genes (Middendorp et al., 2014; Thompson et al., 2017), indicating that enteroid identity was maintained *ex vivo* (Fig. S7B). Enteroids were grown under differentiation-permissive ENR conditions. Upon *Prdm16* ablation, duodenal enteroids displayed the most severe phenotype (Fig. 7D, S7C). By contrast, ileal enteroids lacking *Prdm16* underwent robust budding similar to that of their controls and appeared unaffected overall, with no decrease in survival (Fig. 7D, S7C). Additionally, *Prdm16*-deficient duodenal enteroids were unable to form secondary enteroids, whereas mutant ileal enteroids could be readily passaged, though at a reduced efficiency compared to control (Fig. S7D). Consistent with a reduced role of PRDM16 in the ileal epithelium, the length of epithelial tdTomato$^+$ cell strips was slightly but significantly decreased in the ileum of *Prdm16*-mutant *Lgr5*^{CreERT}; *tdTomato* reporter mice (Fig. S7E).

To determine the effect of *in vivo Prdm16* deletion on enteroid formation from different regions, we isolated duodenal, jejunal or ileal crypts 3 days after administration of tmx. In these experiments, mutant duodenal crypts generated few viable enteroids, and those that survived had a cystic morphology. On the other hand, there was no detectable difference in enteroid formation or viability between control and *Prdm16* mutant ileal crypts (Fig. 7E).

We next sought to determine if tapering PRDM16 expression corresponded to changes in crypt metabolism along the small intestine. Indeed, a large fraction of the FAO genes regulated by PRDM16 (e.g. *Slc27a2, Acsl1, Cpt1a, Cpt2, Acaa2, Hadh, Decr1),* were expressed at high levels in crypts of the duodenum, intermediate levels in jejunum and low levels in the ileum (Fig. 7F). Interestingly, *Ppara* and *Pparg* were also expressed in a similar graded fashion from duodenum to ileum (Fig. 7F). PPARγ, in particular, displayed a striking region-specific expression pattern at both the mRNA and protein level (Fig. 7B,F). Stable isotope tracing showed that palmitate gave the highest contribution to TCA cycle intermediates in duodenal crypts, with lowest contribution in ileal crypts (Fig. 7G, S7F).

These results raised the notion that stem and/or progenitor cells in different intestinal regions may exhibit differential reliance on FAO. To test this, enteroids generated from different regions were treated with etomoxir to block FAO. As above, etomoxir severely impaired the budding of duodenal enteroids (Fig. 7H). Jejunal enteroids were much less affected, while ileal enteroids budded robustly in the presence of etomoxir (Fig. 7H), indicating that intestinal region-specific stem and/or progenitor cells possess different metabolic requirements.

Finally, we performed RNA-seq expression profiling of duodenal, jejunal and ileal crypts to identify region-selective metabolic programs in an unbiased manner. Among genes with higher expression in duodenal (vs. Ileal or Jejunal) crypts, pathway analysis identified a strong enrichment of genes involved in oxidative metabolism, including TCA cycle, electron transport chain, ATP synthase complex and FAO (Fig 7I–J, Table S2A,B). Conversely, ileal crypts showed relatively higher expression of genes involved in acyl chain metabolism and cholesterol biosynthesis (Fig. 7J, S7G, Table S2C). At a global level, a substantial proportion (35%) of the genes that were downregulated by *Prdm16* deletion were also enriched in duodenal vs. ileal crypts (Fig. 7K). The top enriched pathways for these genes were metabolic processes, including “Fatty acid, triacylglycerol, and ketone body metabolism” and “Mitochondrial Fatty Acid Beta-Oxidation” (Fig. 7K, Table S2D,E). Overall, these results demonstrate that crypts from different intestinal regions express divergent metabolic programs and that PRDM16 is a major regulator of the duodenal-specific profile.

Discussion

This study identifies PRDM16 as a critical transcriptional regulator of metabolism and differentiation in the small intestinal crypt. PRDM16 controls the expression of FAO pathway genes and is required for the survival of *Lgr5*+ descendant progenitor cells and epithelial renewal, selectively in the upper region of the small intestine.

PRDM16 and its binding partners PPARα and PPARγ are expressed at high levels in the upper intestine (duodenum and proximal jejunum) and decline distally. FAO genes also follow this expression pattern, accompanied by a higher contribution of FAO to TCA cycle metabolites in upper compared to lower small intestine. This pattern is physiologically rational, as the upper intestine is exposed to the highest level of dietary fat, which is broken down into fatty acids by pancreatic lipases secreted into the duodenum (Iqbal and Hussain, 2009). The specialization of upper intestinal crypt cells for fatty acid catabolism presumably allows these cells to function more efficiently in this metabolic milieu.

A reliance on fatty acid utilization sensitizes duodenal stem and progenitor cells to disruptions in the FAO pathway, as revealed upon *Prdm16*-deletion. Intestinal loss of the FAO enzyme CPT1A causes similar, though less severe phenotypes, including reduced development of mature villus epithelial cells, elevated crypt apoptosis and reduced stem cell function (Mihaylova et al., 2018). The ability of acetate to rescue many of the phenotypic effects of *Prdm16*-deficiency suggests that FAO plays a major role in mediating PRDM16-function. In particular, acetate robustly rescued the growth, survival and renewal capacity of *Prdm16*-mutant duodenal enteroids. However, acetate only partially rescued the budding deficit of *Prdm16*-mutant enteroids, suggesting that PRDM16 controls budding through other mechanisms. In this regard, we noted that PRDM16 regulates other metabolic pathways (Fig. S5M), in addition to FAO, that could contribute to the budding defect of *Prdm16*-mutant enteroids. Presumably, PRDM16 also regulates non-metabolic genes that influence intestinal development.

Our results suggest that PRDM16 plays a critical role in regulating the function of *Lgr5*+ descendant progenitor cells in the upper intestine. PRDM16 is expressed at higher levels in the TA zone of crypts relative to that of *Lgr5*+ stem cells, localized at the crypt base. Moreover, loss of PRDM16 reduced proliferation and triggered apoptosis, specifically in the TA zone, supporting the notion that PRDM16 directly regulates progenitor cell function. Although our most striking phenotypes manifest in the progenitor cell compartment, stem cells lacking *Prdm16* show defects in enteroid forming capacity, and we cannot rule out a proliferation defect in the stem cell compartment. It is therefore possible that *Prdm16* deletion compromises the function of *Lgr5*+ stem cells, which could contribute to the loss of TA progenitors and deficit in epithelial renewal. Additionally, a recent study focusing on the enteroendocrine lineage hierarchy identified *Prdm16* as an enriched transcription factor in enterochromaffin precursors (Gehart et al., 2019). Thus, in addition to broadly regulating metabolic pathways and epithelial renewal in the duodenum, PRDM16 may play other roles in regulating enteroendocrine differentiation.

Both PRDM16 and FAO were dispensable for the formation, growth and renewal of enteroids derived from distal regions of the small intestine. Presumably, progenitor cells in these regions have a higher capacity to utilize other fuel sources or may depend less on oxidative metabolism. Interestingly, ileal crypts selectively expressed genes involved in lipid metabolism and cholesterol biosynthesis, pathways that were recently implicated in regulating intestinal stem cell activity and tumorigenesis (Wang et al., 2018). Overall, our findings highlight the importance of studying intestinal stem cell metabolism in the context of its regional origin rather than in aggregate or from a single region.

An important outstanding question is why duodenal enteroids rely on FAO, considering the availability of other nutrients in the medium. FAO is required in other stem cell niches (Ito et al., 2012; Knobloch et al., 2017), though the reason for this requirement over other pathways is poorly understood. FAO may generate a specific metabolite that is not adequately produced by other pathways and/or affect the sub-cellular distribution of certain metabolites. Metabolism could also influence progenitor function through many epigenetic pathways (Carey et al., 2015; TeSlaa et al., 2016; Wei et al., 2018; Wellen et al., 2009). In this regard, fatty acids can serve as a dominant source of acetyl-CoA for histone modifications (McDonnell et al., 2016). Future studies examining the fate of fatty acid-derived acetyl-CoA in intestinal progenitors will address this question.

This study expands the role of PRDM16 as a metabolic regulator outside of its heavily studied function in brown fat. Many of the PRDM16 binding sites at FAO genes are common to intestine and brown fat, suggesting that PRDM16 has conserved core functions in multiple cell types (Harms et al., 2015; Shapira et al., 2017). PRDM16 has also been linked to metabolism in other stem cell niches, including hematopoietic and neuronal stem cells (Aguilo et al., 2011; Chuikov et al., 2010). *Prdm16*-deficient hematopoietic stem cells show increased respiration and an upregulation of electron transport genes (Corrigan et al., 2018), effects that are not evident in intestine or brown fat. In neuronal progenitors, PRDM16 regulates the expression of *Hgf* to reduce ROS generation (Chuikov et al., 2010). Taken together, these studies highlight multiple pathways through which PRDM16 can regulate stem and progenitor cell activity.

Our studies also suggest an important role for PPARγ in establishing region-specific intestinal metabolism. Notably, PPARγ has a protective effect on the small intestine during injury and in the context of Crohn’s disease (Baregamian et al., 2009; Sugawara et al., 2005). PPARγ also modulates microbiota/host interaction in the small intestine following high fat diet (Tomas et al., 2016). PPARγ and its related family members PPARα and PPARδ are nuclear receptors whose activity can be modulated by a variety of synthetic and proposed natural agonists, including many fatty acids. This property allows PPAR proteins to function as nutritional sensors for integrating environmental changes in fatty acid levels to adaptive changes in metabolic programs. Related to this, PPARδ, whose mRNA is expressed at similar levels as *Ppara* in duodenal crypts, can sense changes in dietary fatty acids as a result of high fat diet and enhance the activity of stem cells and transit-amplifying cells (Beyaz et al., 2016; Mihaylova et al., 2018).

In summary, our studies define PRDM16 as a critical regulator of small intestinal maintenance and uncover an unanticipated role for region-specific metabolic pathways in regulating intestinal epithelial renewal. It will now be important to identify the mechanisms by which specific metabolic programs and metabolites control intestinal stem and progenitor cell activity and to determine if dysregulation of these pathways underlie intestinal disease or dysfunction.

Star Methods

LEAD CONTACT AND MATERIALS AVAILABILITY

Further information and requests for resources and reagents should be directed to and will be fulfilled by the Lead Contact, Patrick Seale (sealep@pennmedicine.upenn.edu). This study did not generate new unique reagents.

EXPERIMENTAL MODEL AND SUBJECT DETAILS

Mice—The following mouse strains were purchased from the Jackson Laboratory: *Rosa26*^{CreERT2} (B6;129-Gt(ROSA)26Sortm1(cre/ERT)Nat/J, RRID: IMSR_JAX:004847); *Lgr5*$^{EGFP\text{-}iREs\text{-}creERT2}$ (B6.129P2-Lgr5tm1(cre/ERT2)Cle/J, RRID :IMSR_JAX:008875); *Rosa26*$^{\text{LoxP-Stop-LoxP-tdTomato}}$ (B6.Cg-Gt(ROSA)26Sortm14 (CAG-tdTomato) Hze/J, RRID: IMSR_JAX:007914); and *p53*$^{loxP/loxP}$ (B6.129P2-Trp53tm1Brn/J, RRID: IMSR_JAX: 008462). The *Prdm16* conditional knockout mouse line was generated by Patrick Seale and Bruce Spiegelman and is available from the Jackson Laboratory: *Prdm16*$^{loxP/loxP}$ (B6.129-Prdm16tm1.1Brsp/J, RRID: IMSR_JAX:024992). All animal work was approved by the University of Pennsylvania's Institutional Animal Care and Use Committee. Mice were housed under the care of University of Pennsylvania University Laboratory Animal Resources (ULAR), which provides both basic husbandry and veterinary care. Animals were specific-pathogen free (SPF) and raised at room temperature on standard chow with a 12-hour light/dark cycle. Both sexes were used for experiments. All experiments were done on adult animals between the ages of 6 to 10 weeks at the onset of the experiment.

METHOD DETAILS

***In Vivo* Treatments—**Tamoxifen (tmx) was used to activate CreER in conditional knockout and lineage-tracing models. For gene knockout, 6-8 week-old-mice (~18-25g) were intraperitoneally injected with tmx (Sigma, stock 20 mg/ml in corn oil) at a dose of 3 mg/d for three consecutive days. For lineage tracing experiments, mice were injected with a single 3 mg dose of tmx. For *in vivo* acetate treatment, drinking water was supplemented with either 150 mM NaCl (Sigma) as control or 150 mM NaAcetate (Sigma). Sibling- or age-matched experimental and control animals were randomly allocated into experimental groups based only on genotype and date of birth. Both female and male mice were analyzed separately for each experiment. All results were consistent between sexes and combined when appropriate. All animal experiments were approved by the University of Pennsylvania's Institutional Animal Care and Use Committee.

Analysis of intestinal barrier function and serum cytokines—For barrier function analysis, mice were gavaged orally with 150 µl of 80 mg/ml fluoroscein isothiocyanate

(FITC) dextran (Sigma) dissolved in sterile PBS (6d after tmx injection). Four hours after gavage, mice were sacrificed, and blood was collected by cardiac puncture. Serum was isolated by centrifugation, diluted 1:10 in PBS and loaded onto a black, opaque bottomed microplate for measurement using a Synergy HT plate reader (BioTek) excited at 485 nm and read at 530 nm. Concentration was determined using a FITC-dextran standard curve. To determine colony formation, whole blood samples were diluted 1:2 or 1:10 in sterile PBS and 100 μl was plated on blood agar plates (Fisher). Plates were incubated at 37°C for 20 hours and colonies were quantified. For cytokine analysis, serum was analyzed by MILLIPLEX Mouse Cytokine/Chemokine Magnetic Bead Immunology Multiplex Assay (Millipore) using a Luminex Flexmap 3D machine in conjunction with the UPenn Human Immunology Core.

Histology and Immunofluorescence—Tissues were fixed in 10% buffered formalin overnight, washed in PBS, dehydrated in ethanol, paraffin-embedded and sectioned. Following deparaffinization, slides were subjected to heat antigen retrieval in a pressure cooker with Bulls Eye Decloaking buffer (Biocare), unless otherwise noted. Slides were incubated in primary antibody overnight and secondary antibody conjugated to peroxidase and then developed using Tyramide Signal Amplification (TSA, Akoya Biosciences). Primary antibodies used for staining were: rabbit anti-PRDM16 (Seale et al., 2011) 1:200, goat anti-Lysozyme C (W-20) (1:50, Santa Cruz Cat# sc-27956, RRID:AB_2138793 (Disc)), rabbit anti-MUC2 (H-300) (1:50, Santa Cruz, Cat#sc-15334, RRID:AB_2146667 no TSA amplification), rabbit anti-MUC2 (1:500, Cloud Clone, Cat#PAA705MU02, no TSA amplification, goat anti-rabbit Alexa 488 secondary), mouse anti-E-cadherin, (1:200, BD Biosciences, Cat#610181, RRID:AB_397580), rabbit anti-KI67 (Abcam Cat#ab16667, RRID:AB_302459, no TSA amplification, goat anti rabbit Alexa 555 secondary), rabbit anti-cleaved NOTCH1 (Val1744) (1:50, Cell Signaling, Cat#4147, RRID:AB_2153348), rabbit anti-cleaved Caspase-3 (1:500, Cell Signaling Cat#9664, RRID: AB_2070042, Borg decloaker), goat anti-GFP (1:500, Abcam, Cat#ab6673, RRID:AB_305643), rabbit anti-RFP (1:250, Rockland Cat#RL600-401-379, RRID:AB_2209751), rabbit anti Chromogranin A (1:500, Abcam, Cat#Ab15160, RRID:AB_301704), rabbit anti-Lysozyme C (1:500, Agilent Cat#A0099, RRID:AB_2341230) and DAPI (1:1000 Roche). Images were captured on a Leica TCS SP8 confocal microscope or Keyence BZ-X700 fluorescent light microscope. Villi length was measured from the top of the crypt to the tip of the villi using the measurement tool in photoshop and pixel length was converted to microns. For lineage tracing experiments, full length small intestines were arranged into tight swiss rolls to maximize cross sectional villus area. Complete swiss rolls were imaged using the multi-image stitching setting of the Keyence BZ-X700 microscope with the 10X objective. Lineage traced experiments were scored blinded.

For enteroid staining, whole enteroids were collected in ice-cold PBS to dissolve Matrigel (Corning) and fixed in 1.5 ml Eppendorf tubes with 4% PFA (EMS) for 15 minutes. Enteroids were washed and blocked with normal donkey serum (Sigma). Primary antibody was incubated overnight, enteroids were washed and secondary antibody was incubated for 1 hour. Primary antibodies were used as listed above. Secondary antibodies were donkey anti-goat IgG, Alexa 488 (1:400 ThermoFisher, Cat#A11055, RRID:AB_2534102), donkey anti-mouse IgG, Alexa 555 (1:200 ThermoFisher, Cat#A31570, RRID:AB_2536180), donkey anti-rabbit IgG, Alexa 647 (1:200 ThermoFisher, Cat#A31573, RRID:AB_2536183), goat anti-rabbit IgG, Alexa 488 (1:400 ThermoFisher, Cat#A11034, RRID:AB_2536180) and DAPI (1:1000, Roche). Enteroids were then washed 3 times and, after the final wash, mounted onto slides in Vectashield (Vector Biolabs) for imaging using a Leica TCS SP8 confocal microscope. All washes were with PBS + 0.1% T riton X with the exception of a final wash in PBS.

Crypt Isolation and culture—Intestinal crypts were isolated according to published methods (Chatterji et al., 2018; Sato et al., 2009). Briefly, 8-10 cm of a specified region of the small intestine were dissected and cleaned with PBS. For duodenum samples, 8 cm was isolated immediately adjacent to the stomach. For jejunum samples, 10 cm was isolated at the midpoint of the small intestine. For ileum samples, 10 cm was isolated immediately adjacent to the cecum. All tissues were kept on ice in Ca^{2+} and Mg^{2+}-free Hank's buffered salt solution (CMF-HBSS, Thermo Fisher) supplemented with 1 mM N-acetyl cysteine (NAC, Sigma). Samples were then transferred to CMF-HBSS containing 10 mM EDTA (Fisher) and 1 mM NAC and rotated for 45 min at 4°C. To dissociate villi and crypts from underlying mesenchyme, tubes were vortexed for 30s following a 30s rest on ice four times (six times for ileal samples). Samples were passed over a 70-μm filter to remove villi, and crypts were gently pelleted. Crypts were resuspended in Basal+ medium (advanced DMEM/F12 medium containing 2 mM Glutamax, 10 mM HEPES, 1X penicillin/streptomycin, 1X N2 supplement, and 1X B27 supplement (all Thermo Fisher), with 5 μM CHIR99021 (Biovision) and 1 mM NAC. Crypts were then counted, pelleted and resuspended at a concentration of 15 crypts/μl in an 80/20 mixture of Matrigel matrix (Corning) and ENR (Basal+ medium also containing 50 ng/mL mouse epidermal growth factor [Preprotech], 60 ng/ml Noggin [Preprotech] and 0.5 μg/ml R-Spondin [Preprotech]) or Intesticult (Stem Cell Technologies) medium. Crypt/matrix mixtures were then plated as droplets into 24- or 96-well plates. After solidification of the matrix, crypt-containing droplets were overlaid with ENR medium. Medium was changed every 48-72 hours. Enteroids were passaged using mechanical dissociation or 2-minute TrypLE Express (Invitrogen) digestion (for Wnt^{high} experiments) every 6-8 days. For experiments involving Wnt^{high} conditions, WENR media was made by supplementing ENR media with 100 ng/ml Wnt3A (R&D Systems) and 10 μM Nicotinamide (Sigma), with 10 μM Y-27632 (Cell Signaling) added for the first 24 hours after passage.

For *ex vivo Prdm16* deletion, 1 μM 4-OHT (Sigma) or vehicle (ethanol, 1:10,000) was added directly to the media for 24 hours. For IFNAR neutralizing antibody experiments, anti-IFNAR antibody (Leinco, Cat#I-401, RRID:AB_2491621) was added directly to enteroid media at a concentration of 1ug/ml immediately after plating. For etomoxir experiments, 50 μM Eto (Sigma) was added directly to the media, and media was refreshed every 48 hours. For acetate rescue experiments, filter sterilized 1M sodium acetate solution was added directly to culture medium to a final concentration of 5 mM. For PPARA and PPARG antagonist experiments, 5uM concentrations of GW9662 or GW6271 (both from Sigma) were added directly to the media. Antagonist treated media was also used to create the 80/20 Matrigel/media mixture. Media was changed every 2 days. DMSO was used as a vehicle control.

For shRNA experiments, PLKO.1-shRNA viral plasmids (see Key Resources Table) were transfected into HEK293T cells along with packaging plasmids pMD2.G and psPAX2 (Addgene #12259 and #12260, a gift from Didier Trono) using Lipofectamine 2000 (Invitrogen). After media change, virus was collected for 48 hours following transfection and concentrated using PEG-It (System Bioscience). Enteroids were infected with concentrated lentivirus using published methods (Andersson-Rolf et al., 2014). Wildtype (B6) enteroids were grown in WENR with 10 μM Nicotinamide (Sigma), with 10 μM Y-27632 (Cell Signaling) to achieve cystic morphology and then trypsinized, split into groups and infected with concentrated control (pLKO-shScr) or *shPrdm16* (pLKO-shPrdm16) lentivirus in the same medium plus 8 mg/ml polybrene. Enteroid fragments were spinoculated in a 48 well plate at 600 x g for 1 hour at 32° C and then incubated at 37° C for 5 hours. Enteroid fragments were spun down, plated in Matrigel and incubated in WENR media for 4 days, followed by 4d treatment with 1 μg/ml Puromycin to select for transduced cells. Enteroids were then transferred to ENR medium to stimulate budding. For *in vivo* crypt knockout experiments, mice were injected with tmx. 3 days later, crypts were isolated and plated (150/per well) in 24 well plates. Enteroid formation was scored on d7.

For passaging experiments, 1 well of enteroids was trypsinized for 2 minutes in TrypLE Express (Invitrogen) to form fragments of ~10-20 cells and plated into 4 wells. The number of enteroids recovered from each well was quantified. Enteroids were removed from Matrigel and resuspended in PBS droplets for counting if numbers were high or accurate counts could not be obtained within the Matrigel droplet. The 4 wells plated from each parent well were averaged and represent an N of 1.

All quantifications were performed by taking images of at least 3 wells at 10× magnification using Leica DM IL LED inverted light microscope with a Canon EOS Rebel T1i 15.1 MP CMOS Digital SLR Camera. For enteroid/bud growth, enteroids were photographed over time and the same enteroids were measured using the Photoshop measuring tool. Enteroid fields to photograph were chosen randomly by marking the bottom of culture plate well with 3 dots. All images over the timecourse were centered around the dots and taken in multiple focal planes to allow for tracking of enteroids over time. For buds, measurements were from tip to enteroid body as shown in example images in Fig. S4B. For spheroids/enteroids, measurements made of widest diameters, as shown in example images in Fig. S4G. All replicate measures were converted to percent growth of single enteroids over time, aggregated and graphed. Viable enteroids were defined as having a clear and unbroken epithelial cell border. Non-viable enteroids were counted if they could be identified as viable at earlier timepoints. “Non-budding” or spheroid enteroids were defined as have a round or oval shape with no protrusions of the epithelium. “Budding” was defined as an epithelial protrusion representing a crypt emerging from the spheroid body.

RNA Extraction and qRT-PCR.—Total RNA was extracted from isolated crypts or enteroids (following one ice cold PBS wash to dissolve Matrigel) using TRIzol (Invitrogen) combined with Purelink RNA Mini columns (Fisher) and then reverse transcribed into cDNA using the ABI High-Capacity cDNA Synthesis kit (ABI). Real-time PCR was performed on an ABI7900HT PCR machine using SYBR green fluorescent dye (Applied Biosystems). Fold changes were calculated using the delta delta CT method, with Tata Binding Protein (TBP) serving as a normalization control. Primer sequences can be found in Table S3.

Flow Cytometry—Intestines were opened and cleaned in PBS, followed by soaking in HBSS with 30mM EDTA and 1.5mM DTT (Roche) on ice for 20 minutes. Intestines were shifted to HBSS with 30mM EDTA and rotated at 37C for 8 minutes, with shaking every 2 minutes. Samples were strained through a 70 μm filter and pelleted at 300g for 5 minutes at 4°C. Pellets were resuspended in 5 ml DMEM with 0.3U/ml Dispase II (Roche) and rotated at 37°C for 10 min with shaking every 2 min and then quenched with FBS + 10 U/ml DNase (Roche), followed by filtration through a 40 μM filter. Samples were again pelleted at 500g for 5 min at 4°C. Pellets were suspended in 5 ml room temperature Red Blood Cell Lysis Buffer (Biolegend) for 4 min and quenched with DMEM +10% FBS (Omega). Samples were pelleted at 500g for 5 minutes at 4°C and resuspended in FACS medium (FluoroBrite DMEM (Gibco) with 3% FBS, 10U/ml DNase, 10uM Y27632). Samples were stained with: anti-CD45 PE (1:100, Biolegend, Cat#103106, RRID:AB_312971), anti-Ter119 PE (1:100, Biolegend, Cat#116207, RRID:AB_313708), anti- CD31 PE (1:100, Biolegend, Cat#102407, RRID:AB_312902), anti- Epcam APC (1:100, EBiosciences, Cat#17-5791-80, RRID:AB_2734965), anti- CD24 Pacific Blue (1:100, Biolegend, Cat#101820, RRID:AB_572011), anti- c-kit APC-Cy7 (1:100, Biolegend, Cat#105825, RRID:AB_1626280) and 7-AAD viability stain (1:10, Biolegend) for 30 minutes at 4C with rocking. Cells were sorted on an BD FACs Aria II with compensation being performed at the time of acquisition in Diva software by using AbC Total Compensation beads (Molecular Probes) for single-color staining and isolated crypt cells for negative staining and fluorescence (7-AAD and GFP). GFP^{hi} stem cells, GFP^{low} progenitor cells and Paneth cells were isolated according to the sorting strategy described by (Beyaz et al., 2016). Stem cells were identified as *Lgr5*-GFP^{hi}, Epcam^{pos}, CD24^{low}, C-KIT^{neg}/ CD31^{neg}, Ter119^{neg},CD45^{neg},7-AAD^{neg}. GFP^{low} progenitors were identified as GFP^{low}, Epcam^{pos}, CD24^{low}, C-KIT^{neg} /CD31^{neg}, Ter119^{neg}, CD45^{neg}, 7-AAD^{neg}. Paneth cells were isolated as CD24^{hi}, C-KIT^{hi}, SSC^{hi}, GFP^{neg}, CD31^{neg},Ter119^{neg},CD45^{neg},7-AAD^{neg}. Cells were collected in basal crypt culture medium supplemented with 10% FBS, 10 U/ml DNase and 10 μM Y27632. For RNA isolation after sorting, FACS isolated cells were pelleted at 500g and RNA was isolated using Trizol extraction and an Arcturus PicoPure RNA Isolation Kit. cDNA synthesis was performed as above.

Colony Formation Assays—Sorted cells were gently pelleted (500g) and resuspended in complete medium at a concentration of 100 cells/μl. For Stem cell and Paneth cell mixing experiments, cells were mixed at a 1:1 ratio, pelleted again and resuspended at a concentration of 1000 stem cells/10 μl Matrigel with 20% complete medium. Matrigel was solidified for 10 min and overlaid with medium. For stem cell assays without Paneth cells, 1000 cells/10 μl Matrigel were plated with WENR media. Enteroid formation was quantified after 4d and 14d. All colony formation experiments reported were repeated 3 or more times.

RNA-seq analysis—RNA-seq libraries were generated using a Truseq RNA Sample Preparation kit (Version 2, Illumina). RNA-seq was performed by the University of Pennsylvania Next Gen Sequencing Core on a HiSeq 2500 high output sequencer using 100 base pair single-end reads. RNA-seq reads were aligned to UCSC mm9 using STAR pipeline (Dobin et al., 2013) allowing unique mapping only. All samples had uniquely mapped read percentages between 81% and 89% (Table S2F). Tags were counted for each gene using featureCounts (Liao et al., 2014). Differential gene expression was done using edgeR (Robinson et al., 2010). Differential expression was determined using the EdgeR software package using quantile normalized log2 fold change of mutant divided by control. 0-1 False Discovery Rates were calculated from the p-value using a Benjamini-Hochberg correction. Upregulated genes with a FDR <0.05 or downregulated genes with an FDR <0.05 were analyzed using ToppFun Reactome Pathways tool (https://toppgene.cchmc.org/enrichment.jsp) (Chen et al., 2009); FDR<0.1, between 1 and 2000 genes using RefSeq ID entry. Heat maps were created using Morpheus (https://software.broadinstitute.org/morpheus). RNA-seq data sets have been deposited in Gene Expression Omnibus (GEO) with the following accession number: GSE121009. For regional crypt RNA-seq, total RNA was isolated from purified crypts of the duodenum (top 8cm), jejunum (10 cm around small intestinal midpoint) and ileum (bottom 10 cm) in C57/B6J mice. Total RNA was sent to Novogene for library preparation and sequencing. Libraries were prepared using the NEB Next Ultra RNA Library Prep Kit and sequenced on a HiSeqX Ten (150 base pair, paired-end reads). FASTQ files were aligned to mm10 by using STAR-2.5.2a, and all samples had uniquely mapped read percentages between 81% and 87%. Differential gene expression was analyzed by using the R package DESeq2. For comparison of overlap in *Prdm16* control vs Mut and Duodenum vs Ileum differentially expressed gene sets, FASTQ files for control vs *Prdm16* KO animals were aligned to mm10 by using STAR-2.5.2a, and differential gene expression was analyzed by using the R package DESeq2. For the control vs Mut comparison, gene lists were generated with padj<0.2 and log2 Fold Change > 0.5 for upregulated genes or <−0.5 for downregulated genes (in the control compared to the KO). For the Duodenum vs Jejunum comparison, gene lists were generated with padj<0.1 and log2 Fold Change > 0.5 for upregulated genes or <−0.5 for downregulated genes (in the Duodenum compared to the Ileum). Enrichment analysis was performed using the Reactome tool (https://toppgene.cchmc.org/enrichment.jsp) analysis on the genes that were upregulated (or downregulated) in both the control vs mutant and Duodenum vs Ileum comparison (Chen et al., 2013; Kuleshov et al., 2016). All RNAseq data sets includes 3 biological replicates.

^{13}C-Glucose and ^{13}C-Palmitate Metabolomics Labeling and LC/MS—For U-13C-Palmitate labeling, crypts were isolated from the specified small intestine regions. Control (*Prdm16*$^{loxP/loxP}$) or global *Prdm16* mutant (*Rosa26*^{CreERT2}; *Prdm16*$^{loxP/loxP}$) mice were sacrificed 72h following initial tmx injection. Crypts were counted, and 2,000 crypts were seeded per well of a 24 well plate coated in a 10% Matrigel/90% RPMI mixture. Crypts were overlaid with 500 μl RPMI media containing growth factors (EGF, Noggin, R-spondin), 5 μM CHIR99021, 1 mM NAC, 1 μg/ml L-carnitine (Sigma) and 150 μM U-^{13}C$_{16}$-Palmitatic-Acid (Cambridge) conjugated to fatty acid-free BSA. Crypts were incubated for 90 min and then 3 wells were combined and spun down in ice cold labeling medium to remove Matrigel and resuspended in 800 μl of extraction buffer (40% methanol

(VWR), 40% Acetonitrile (Fisher), 20% water (Fisher), all LC/MS grade with 0.5% formic acid). Samples were vortexed and placed on ice. Within 5 min, samples were neutralized by adding 15% ammonium bicarbonate (Sigma, amount determined before each experiment), vortexed again and returned to ice for 10 min. Samples were cleared in a cold centrifuge at max speed for 10 min. Supernatants were collected and then dried in a vacuum dryer or under a stream of nitrogen, followed by resuspension in 100 μl LC/MS grade water for mass spec analysis.

For glucose labeling, enteroids were grown in 50% Matrigel, 50% media and treated with 1 μM 4-OHT for 48 hours prior to exposure to labeled glucose. To make labeling media, Dulbecco's MEM (DMEM) F-12, lacking Amino Acids, L-Glutamine, Glucose and Sodium Pyruvate (US Biologicals) was prepared and supplemented with 1X essential and non-essential amino acids (ThermoFisher), 1 μg/ml glutathione (Sigma) and 29 mM sodium bicarbonate (Sigma) and 17.5 mM $^{13}C_6$ Glucose (Cambridge). This media was used as a base for complete enteroid media (substituted for Advanced DMEM/F12), which was prepared as described above. Enteroids were incubated for 4h in labeled glucose. Enteroids were then recovered by dissolving Matrigel in ice cold medium, spinning briefly and resuspending in extraction buffer and processing as described above.

Cell extracts were analyzed by LC-MS analysis on a Q Exactive PLUS hybrid quadrupole-orbitrap mass spectrometer (Thermo Scientific) coupled to hydrophilic interaction chromatography (HILIC) via electrospray ionization. The LC separation was performed on a XBridge BEH Amide column (150 mm χ 2.1 mm, 2.5 μM particle size, Waters, Milford, MA) using a gradient of solvent A (95%:5% H2O:acetonitrile with 20 mM ammonium acetate, 20 mM ammonium hydroxide, pH 9.4), and solvent B (100% acetonitrile). The gradient was 0 min, 85% B; 2 min, 85% B; 3 min, 80% B; 5 min, 80% B; 6 min, 75% B; 7 min, 75% B; 8 min, 70% B; 9 min, 70% B; 10 min, 50% B; 12 min, 50% B; 13 min, 25% B; 16 min, 25% B; 18 min, 0% B; 23 min, 0% B; 24 min, 85% B; 30 min, 85% B. The flow rate was 150 μL min–1 . Injection volume was 10 μL and autosampler and column temperature were 4 °C; and 25 °C, respectively. The MS scans were in both positive and negative ion mode with a resolution of 70,000 at m/z 200. The automatic gain control (AGC) target was $5 \chi 10^5$ and the scan range was 75–1000 at 1Hz. Data were analyzed using MAVEN software (Melamud et al., 2010). Isotope labeling was corrected for natural abundance of ^{13}C using an in-house correction code in R (Su et al., 2017). Percent carbon with ^{13}C label was calculated in Excel using the equation [(%M+1) + 2* (%M+2) + 3*(%M+3) + 4*(%M+4) + 5*(%M+5) + 6*(%M+6)]/6 *100 (for citrate/isocitrate) and [(%M+1) + 2* (%M+2) + 3*(%M+3) + 4*(%M+4) + 5*(%M+5) /5*100] (for α-ketoglutarate) (Fendt et al., 2013).

Human Protein Atlas RNA-seq—Human RNA-seq data from a panel of tissues was accessed via Human Protein Atlas (https://www.proteinatlas.org). Gene level RNA-seq (Uhlen et al., 2015) was downloaded from https://www.proteinatlas.org/download/rna_tissue.tsv.zip.

Chromatin Immunoprecipitation—ChIP analysis was performed as previously described (Shapira et al., 2017). Crypts were isolated and fixed with 1.1% formaldehyde for

15 min at room temperature and then quenched with 2.5 M glycine for 5 mins at room temperature. Samples were washed with PBS, pelleted and resuspended in ChIP lysis buffer (0.6% SDS, 1% Triton X-100, 0.15 M NaCl, 1 mM EDTA, 20 mM Tris at pH 8) with protease inhibitors (Roche) and 1 mM PMSF. Crypts were sonicated to shear chromatin using an Active Motif EpiShear platform (8 minutes active time, 30 sec on, 20 sec off, amplitude 25%). To a achieve a final concentration of 0.1% SDS, chromatin was diluted 1:6 with ChIP dilution buffer (1% Triton X-100, 0.15 M NaCl, 1 mM EDTA, 20 mM Tris at pH 8). Inputs were removed, and primary antibodies were added for overnight incubation at 4°C with rotation. Antibodies used were 3 μg of anti-PRDM16 (P. Seale, made in house), 4 μg of anti-PPARα H98 (Santa Cruz, Cat#sc-9000X, RRID:AB_2165737), 4 μg of anti-PPARγ H100 (Santa Cruz, Cat#sc-7196 X, RRID:AB_654710), 10 μl of anti PPARγ A1 (Cell Signaling, Cat#2443S, RRID:AB_823598), 3 μg anti-H3K27Ac (Active Motif, Cat#39133, RRID:AB_2561016) and 3 μg of normal rabbit IgG (Cell Signaling, RRID:AB_1031062). Protein A Sepharose beads (GE healthcare) were then added for 4 hours at 4°C Samples were washed twice with wash buffer 1 (0.1% SDS, 0.1% NaDOC, 1% Triton X-100, 0.15 M NaCl, 1 mM EDTA, 20 mM Tris at pH 8), once with wash buffer 2 (0.1% SDS, 0.1% NaDOC, 1% Triton X-100, 0.5 M NaCl, 1 mM EDTA, 20 mM Tris at pH 8), once with wash buffer 3 (0.25 M LiCl, 0.5% NaDOC, 0.5% NP-40, 1 mM EDTA, 20 mM Tris at pH 8), and twice with wash buffer 4 (1 mM EDTA, 20 mM Tris at pH 8). Samples were then eluted from beads with warm 100 mM $NaHCO_3$/1% SDS buffer. Samples were reverse cross-linked overnight at 65°C with RN ase A and then treated with proteinase K and column purified (Clontech NucleoSpin). ChIP enrichment was calculated as percent of input. H3K27Ac ChIP control and global *Prdm16* mutant samples were prepared as ChIP-seq libraries using the NEBNext ChIP-seq DNA Sample Prep Master Mix Set 1 (NEB) according to manufacturer instructions. PRDM16 ChIP control and global mutant samples were prepared as ChIP-seq libraries using the NEBNext Ultra II DNA Library Prep kit with Sample Purification Beads. Adaptor and primer sequences can be found in the Key Resources table. Libraries were sequenced using a HiSeq 4000 high output sequencer with 100 base pair, single end reads. ChlP-seq data sets have been deposited in Gene Expression Omnibus (GEO). For H3K27Ac, ChIP-seq data was analyzed, using downsampling to match sequencing depth between control and global *Prdm16* mutant H3K27Ac samples. All bigwig files for ChIP-seq data were generated using Homer and bedGraphToBigWig command in RPM scale. Sequencing reads were aligned to mm9 using bowtie (Langmead et al., 2009). Peak calling was done by ‘findPeak’ in Homer (Heinz et al., 2010) using an option “-style histone -nfr”. Peaks from control and Prdm16 mutant were pooled to make a master peak set and overlapping peaks were merged if their center distance was <100bp. These signals were further normalized using ‘normalize.loess’ in affy, R package. Differential H3K27ac peaks were defined by 1.5-fold-change cut off. De novo motif search and motif scan were performed using Homer. For PRDM16 ChIP-seq, ChIP-seq reads were aligned to UCSC mm9 using the STAR pipeline. All samples had uniquely mapped read percentages between 74% and 81%. Biological replicates were pooled after deduplicating. Prdm16 peaks were called against KO as a control using Homer (Heinz et al., 2010). To examine the relationship between PRDM16 peaks and gene expression, we measured the distances from transcription start sites of expressed genes to the closest PRDM16 binding sites then compared them by

grouping *Prdm16* deletion-induced gene expression changes. ChIP-Seq experiments included 2 biological replicates. ChIP qPCR experiments included 3 or more replicates.

Western blot—Protein extracts were prepared by resuspending isolated crypt pellets in RIPA buffer with protease inhibitors (Roche). Samples were sonicated using a Diagenode Bioruptor for 2.5 minutes (30 sec on, 30 sec off, high) and protein was quantified using a standard DC assay (BioRad). Proteins were separated in 4–12% Bis–Tris NuPAGE gels (Invitrogen) and transferred to low-fluorescent PVDF membranes using either a standard wet transfer (90 minutes at 325 amps for PRDM16) or a BioRad Transblot Turbo system (for PPARγ). Antibodies used were as follows: anti-PRDM16, 1:1000 (Seale et al., 2011), anti-PPARγ 1:1000 (Cell Signaling, Cat#2443S, RRID:AB_823598), anti-p53 1:1000 (Cell Signaling, Cat#2524S, RRID:AB_331743), anti-αTUB 1:10,000 (DM1A) (Sigma, Cat#CP06 RRID:AB_477583), and anti-GAPDH 1:10,000 (Thermo, Cat#MA515738, RRID:AB_10977387). Blots were developed using either film or LiCor. For film, blots were incubated with either anti-rabbit-IgG-HRP (Cell Signaling, Cat#7074S, RRID:AB_2099233) or anti-mouse IgG-HRP (Cell Signaling, Cat#7076S, RRID:AB_330924) secondary antibodies, developed using SuperSignal West Dura ECL (Fisher). Alternatively, blots were incubated with the LiCor secondaries anti-mouse IgG IRDye 680RD (Li-Cor, Cat#926-68072, RRID:AB_10953628) and anti-rabbit IgG, donkey, IRDye 800CW (Li-Cor, Cat#926-32213, RRID:AB_621848) and imaged on a LiCOR Odyssey imaging system.

Quantification of fluorescent images—For quantification of area on immunofluorescence images (used for tdTomato and lysozyme), channels of interest were opened in ImageJ. A gaussian blur was applied to the image and threshold was set to identify positive pixels. The image was converted to a mask and particles were analyzed to calculate area. Images were acquired on blinded samples.

QUANTIFICATION AND STATISTICAL ANALYSIS

All experiments reported in this study were repeated at least two independent times. Unless otherwise specified in the main text or figure legends, all sample numbers (n) listed in legends represent biological replicates. For murine enteroid assays, 2-4 wells per group with at least 3 different mice were analyzed. All center values shown in graphs refer to the mean. For analysis of the statistical significance of differences between two groups, two-tailed unpaired Student’s t tests were used. For analysis of three or more groups, a one-way Anova was used. For statistical analysis of two outcomes (i.e. budding, viability), a categorical Fisher exact test was used. No samples or animals were excluded from analysis with the exception of one $^{13}C_{16}$-palmitate metabolomic sample from the control group, which was incorrectly extracted and quenched during processing. Sample size estimates were not used. Animals were randomly assigned to groups. Lineage tracing measurements were performed blinded.

DATA AND CODE AVAILABILITY

The accession number for the high throughput sequencing data reported in this paper is GEO: GSE121014.

Supplementary Material

Refer to Web version on PubMed Central for supplementary material.

Acknowledgements

We thank members of the Seale laboratory for helpful discussions and careful reading of the manuscript. We thank M. Zhou, R. Fadnavis, and C. Ghougasian for technical assistance and Chi Dang for helpful comments. Thanks to the Functional Genomics Core of the Penn Diabetes Center (DK19525) for sequencing, the Human Immunology Core (P30-Ca016520) for Luminex analysis, and the UPenn Histology and Gene Expression Core. This work was supported by: start-up funds provided by the UPenn Institute for Diabetes, Obesity and Metabolism, NIH grants DK10300802 and DK107589 to P.S.; DK10574303 to R.R.S. and a pilot grant from the Center for Molecular Studies in Digestive and Liver Diseases (NIH P30 DK050306).

References

Aguilo F, Avagyan S, Labar A, Sevilla A, Lee DF, Kumar P, Lemischka IR, Zhou BY, and Snoeck HW (2011). Prdm16 is a physiologic regulator of hematopoietic stem cells. Blood 117, 5057–5066. [PubMed: 21343612]

Andersson-Rolf A, Fink J, Mustata RC, and Koo BK (2014). A video protocol of retroviral infection in primary intestinal organoid culture. J Vis Exp, e51765. [PubMed: 25146755]

Baregamian N, Mourot JM, Ballard AR, Evers BM, and Chung DH (2009). PPAR-gamma agonist protects against intestinal injury during necrotizing enterocolitis. Biochem Biophys Res Commun 379, 423–427. [PubMed: 19114032]

Barker N, van Es JH, Kuipers J, Kujala P, van den Born M, Cozijnsen M, Haegebarth A, Korving J, Begthel H, Peters PJ, et al. (2007). Identification of stem cells in small intestine and colon by marker gene Lgr5. Nature 449, 1003–1007. [PubMed: 17934449]

Beyaz S, Mana MD, Roper J, Kedrin D, Saadatpour A, Hong SJ, Bauer-Rowe KE, Xifaras ME, Akkad A, Arias E, et al. (2016). High-fat diet enhances stemness and tumorigenicity of intestinal progenitors. Nature 531, 53–58. [PubMed: 26935695]

Carey BW, Finley LW, Cross JR, Allis CD, and Thompson CB (2015). Intracellular alpha-ketoglutarate maintains the pluripotency of embryonic stem cells. Nature 518, 413–416. [PubMed: 25487152]

Chatterji P, Hamilton KE, Liang S, Andres SF, Wijeratne HRS, Mizuno R, Simon LA, Hicks PD, Foley SW, Pitarresi JR, et al. (2018). The LIN28B-IMP1 post-transcriptional regulon has opposing effects on oncogenic signaling in the intestine. Genes Dev 32, 1020–1034. [PubMed: 30068703]

Chen EY, Tan CM, Kou Y, Duan Q, Wang Z, Meirelles GV, Clark NR, and Ma’ayan A (2013). Enrichr: interactive and collaborative HTML5 gene list enrichment analysis tool. BMC Bioinformatics 14, 128. [PubMed: 23586463]

Chen J, Bardes EE, Aronow BJ, and Jegga AG (2009). ToppGene Suite for gene list enrichment analysis and candidate gene prioritization. Nucleic Acids Res 37, W305–311. [PubMed: 19465376]

Chuikov S, Levi BP, Smith ML, and Morrison SJ (2010). Prdm16 promotes stem cell maintenance in multiple tissues, partly by regulating oxidative stress. Nat Cell Biol 12, 999–1006. [PubMed: 20835244]

Cohen P, Levy JD, Zhang Y, Frontini A, Kolodin DP, Svensson KJ, Lo JC, Zeng X, Ye L, Khandekar MJ, et al. (2014). Ablation of PRDM16 and beige adipose causes metabolic dysfunction and a subcutaneous to visceral fat switch. Cell 156, 304–316. [PubMed: 24439384]

Corrigan DJ, Luchsinger LL, Justino de Almeida M, Williams LJ, Strikoudis A, and Snoeck HW (2018). PRDM16 isoforms differentially regulate normal and leukemic hematopoiesis and inflammatory gene signature. J Clin Invest 128, 3250–3264. [PubMed: 29878897]

Dobin A, Davis CA, Schlesinger F, Drenkow J, Zaleski C, Jha S, Batut P, Chaisson M, and Gingeras TR (2013). STAR: ultrafast universal RNA-seq aligner. Bioinformatics 29, 15–21. [PubMed: 23104886]

Fendt SM, Bell EL, Keibler MA, Davidson SM, Wirth GJ, Fiske B, Mayers JR, Schwab M, Bellinger G, Csibi A, et al. (2013). Metformin decreases glucose oxidation and increases the dependency of prostate cancer cells on reductive glutamine metabolism. Cancer Res 73, 4429–4438. [PubMed: 23687346]

Folmes CD, Dzeja PP, Nelson TJ, and Terzic A (2012). Metabolic plasticity in stem cell homeostasis and differentiation. Cell Stem Cell 11, 596–606. [PubMed: 23122287]

Gehart H, van Es JH, Hamer K, Beumer J, Kretzschmar K, Dekkers JF, Rios A, and Clevers H (2019). Identification of Enteroendocrine Regulators by Real-Time Single-Cell Differentiation Mapping. Cell 176, 1158–1173 e1116. [PubMed: 30712869]

Harms MJ, Lim HW, Ho Y, Shapira SN, Ishibashi J, Rajakumari S, Steger DJ, Lazar MA, Won KJ, and Seale P (2015). PRDM16 binds MED1 and controls chromatin architecture to determine a brown fat transcriptional program. Genes Dev 29, 298–307. [PubMed: 25644604]

Heinz S, Benner C, Spann N, Bertolino E, Lin YC, Laslo P, Cheng JX, Murre C, Singh H, and Glass CK (2010). Simple combinations of lineage-determining transcription factors prime cis-regulatory elements required for macrophage and B cell identities. Mol Cell 38, 576–589. [PubMed: 20513432]

Hondares E, Rosell M, Diaz-Delfin J, Olmos Y, Monsalve M, Iglesias R, Villarroya F, and Giralt M (2011). Peroxisome proliferator-activated receptor alpha (PPARalpha) induces PPARgamma coactivator 1alpha (PGC-1alpha) gene expression and contributes to thermogenic activation of brown fat: involvement of PRDM16. J Biol Chem 286, 43112–43122. [PubMed: 22033933]

Inoue M, Iwai R, Tabata H, Konno D, Komabayashi-Suzuki M, Watanabe C, Iwanari H, Mochizuki Y, Hamakubo T, Matsuzaki F, et al. (2017). Prdm16 is crucial for progression of the multipolar phase during neural differentiation of the developing neocortex. Development 144, 385–399. [PubMed: 27993981]

Iqbal J, and Hussain MM (2009). Intestinal lipid absorption. Am J Physiol Endocrinol Metab 296, E1183–1194. [PubMed: 19158321]

Ito K, Carracedo A, Weiss D, Arai F, Ala U, Avigan DE, Schafer ZT, Evans RM, Suda T, Lee CH, et al. (2012). A PML-PPAR-delta pathway for fatty acid oxidation regulates hematopoietic stem cell maintenance. Nat Med 18, 1350–1358. [PubMed: 22902876]

Ito K, and Ito K (2016). Metabolism and the Control of Cell Fate Decisions and Stem Cell Renewal. Annu Rev Cell Dev Biol 32, 399–409. [PubMed: 27482603]

Kajimura S, Seale P, Tomaru T, Erdjument-Bromage H, Cooper MP, Ruas JL, Chin S, Tempst P, Lazar MA, and Spiegelman BM (2008). Regulation of the brown and white fat gene programs through a PRDM16/CtBP transcriptional complex. Genes Dev 22, 1397–1409. [PubMed: 18483224]

Knobloch M, Pilz GA, Ghesquiere B, Kovacs WJ, Wegleiter T, Moore DL, Hruzova M, Zamboni N, Carmeliet P, and Jessberger S (2017). A Fatty Acid Oxidation-Dependent Metabolic Shift Regulates Adult Neural Stem Cell Activity. Cell Rep 20, 2144–2155. [PubMed: 28854364]

Kuleshov MV, Jones MR, Rouillard AD, Fernandez NF, Duan Q, Wang Z, Koplev S, Jenkins SL, Jagodnik KM, Lachmann A, et al. (2016). Enrichr: a comprehensive gene set enrichment analysis web server 2016 update. Nucleic Acids Res 44, W90–97. [PubMed: 27141961]

Liao Y, Smyth GK, and Shi W (2014). featureCounts: an efficient general purpose program for assigning sequence reads to genomic features. Bioinformatics 30, 923–930. [PubMed: 24227677]

McDonnell E, Crown SB, Fox DB, Kitir B, Ilkayeva OR, Olsen CA, Grimsrud PA, and Hirschey MD (2016). Lipids Reprogram Metabolism to Become a Major Carbon Source for Histone Acetylation. Cell Rep 17, 1463–1472. [PubMed: 27806287]

Melamud E, Vastag L, and Rabinowitz JD (2010). Metabolomic analysis and visualization engine for LC-MS data. Anal Chem 82, 9818–9826. [PubMed: 21049934]

Middendorp S, Schneeberger K, Wiegerinck CL, Mokry M, Akkerman RD, van Wijngaarden S, Clevers H, and Nieuwenhuis EE (2014). Adult stem cells in the small intestine are intrinsically programmed with their location-specific function. Stem Cells 32, 1083–1091. [PubMed: 24496776]

Mihaylova MM, Cheng CW, Cao AQ, Tripathi S, Mana MD, Bauer-Rowe KE, Abu-Remaileh M, Clavain L, Erdemir A, Lewis CA, et al. (2018). Fasting Activates Fatty Acid Oxidation to Enhance Intestinal Stem Cell Function during Homeostasis and Aging. Cell Stem Cell 22, 769–778 e764. [PubMed: 29727683]

Ohno H, Shinoda K, Ohyama K, Sharp LZ, and Kajimura S (2013). EHMT1 controls brown adipose cell fate and thermogenesis through the PRDM16 complex. Nature 504, 163–167. [PubMed: 24196706]

Ohno H, Shinoda K, Spiegelman BM, and Kajimura S (2012). PPARgamma agonists induce a white-to-brown fat conversion through stabilization of PRDM16 protein. Cell Metab 15, 395–404. [PubMed: 22405074]

Pinheiro I, Margueron R, Shukeir N, Eisold M, Fritzsch C, Richter FM, Mittler G, Genoud C, Goyama S, Kurokawa M, et al. (2012). Prdm3 and Prdm16 are H3K9me1 methyltransferases required for mammalian heterochromatin integrity. Cell 150, 948–960. [PubMed: 22939622]

Porta C, Hadj-Slimane R, Nejmeddine M, Pampin M, Tovey MG, Espert L, Alvarez S, and Chelbi-Alix MK (2005). Interferons alpha and gamma induce p53-dependent and p53-independent apoptosis, respectively. Oncogene 24, 605–615. [PubMed: 15580300]

Potten CS, and Loeffler M (1990). Stem cells: attributes, cycles, spirals, pitfalls and uncertainties. Lessons for and from the crypt. Development 110, 1001–1020. [PubMed: 2100251]

Robinson MD, McCarthy DJ, and Smyth GK (2010). edgeR: a Bioconductor package for differential expression analysis of digital gene expression data. Bioinformatics 26, 139–140. [PubMed: 19910308]

Rodriguez-Colman MJ, Schewe M, Meerlo M, Stigter E, Gerrits J, Pras-Raves M, Sacchetti A, Hornsveld M, Oost KC, Snippert HJ, et al. (2017). Interplay between metabolic identities in the intestinal crypt supports stem cell function. Nature 543, 424–427. [PubMed: 28273069]

Sato T, Vries RG, Snippert HJ, van de Wetering M, Barker N, Stange DE, van Es JH, Abo A, Kujala P, Peters PJ, et al. (2009). Single Lgr5 stem cells build crypt-villus structures in vitro without a mesenchymal niche. Nature 459, 262–265. [PubMed: 19329995]

Schell JC, Wisidagama DR, Bensard C, Zhao H, Wei P, Tanner J, Flores A, Mohlman J, Sorensen LK, Earl CS, et al. (2017). Control of intestinal stem cell function and proliferation by mitochondrial pyruvate metabolism. Nat Cell Biol 19, 1027–1036. [PubMed: 28812582]

Schug ZT, Vande Voorde J, and Gottlieb E (2016). The metabolic fate of acetate in cancer. Nat Rev Cancer 16, 708–717. [PubMed: 27562461]

Seale P, Bjork B, Yang W, Kajimura S, Chin S, Kuang S, Scime A, Devarakonda S, Conroe HM, Erdjument-Bromage H, et al. (2008). PRDM16 controls a brown fat/skeletal muscle switch. Nature 454, 961–967. [PubMed: 18719582]

Seale P, Conroe HM, Estall J, Kajimura S, Frontini A, Ishibashi J, Cohen P, Cinti S, and Spiegelman BM (2011). Prdm16 determines the thermogenic program of subcutaneous white adipose tissue in mice. J Clin Invest 121, 96–105. [PubMed: 21123942]

Shapira SN, Lim HW, Rajakumari S, Sakers AP, Ishibashi J, Harms MJ, Won KJ, and Seale P (2017). EBF2 transcriptionally regulates brown adipogenesis via the histone reader DPF3 and the BAF chromatin remodeling complex. Genes Dev 31, 660–673. [PubMed: 28428261]

Shimada IS, Acar M, Burgess RJ, Zhao Z, and Morrison SJ (2017). Prdm16 is required for the maintenance of neural stem cells in the postnatal forebrain and their differentiation into ependymal cells. Genes Dev 31, 1134–1146. [PubMed: 28698301]

Shrum B, Anantha RV, Xu SX, Donnelly M, Haeryfar SM, McCormick JK, and Mele T (2014). A robust scoring system to evaluate sepsis severity in an animal model. BMC Res Notes 7, 233. [PubMed: 24725742]

Su X, Lu W, and Rabinowitz JD (2017). Metabolite Spectral Accuracy on Orbitraps. Anal Chem 89, 5940–5948. [PubMed: 28471646]

Sugawara K, Olson TS, Moskaluk CA, Stevens BK, Hoang S, Kozaiwa K, Cominelli F, Ley KF, and McDuffie M (2005). Linkage to peroxisome proliferator-activated receptor-gamma in SAMP1/YitFc mice and in human Crohn's disease. Gastroenterology 128, 351–360. [PubMed: 15685547]

Takeda N, Jain R, LeBoeuf MR, Wang Q, Lu MM, and Epstein JA (2011). Interconversion between intestinal stem cell populations in distinct niches. Science 334, 1420–1424. [PubMed: 22075725]

TeSlaa T, Chaikovsky AC, Lipchina I, Escobar SL, Hochedlinger K, Huang J, Graeber TG, Braas D, and Teitell MA (2016). alpha-Ketoglutarate Accelerates the Initial Differentiation of Primed Human Pluripotent Stem Cells. Cell Metab 24, 485–493. [PubMed: 27476976]

Thompson CA, Wojta K, Pulakanti K, Rao S, Dawson P, and Battle MA (2017). GATA4 Is Sufficient to Establish Jejunal Versus Ileal Identity in the Small Intestine. Cell Mol Gastroenterol Hepatol 3, 422–446. [PubMed: 28462382]

Tomas J, Mulet C, Saffarian A, Cavin JB, Ducroc R, Regnault B, Kun Tan C, Duszka K, Burcelin R, Wahli W, et al. (2016). High-fat diet modifies the PPAR-gamma pathway leading to disruption of microbial and physiological ecosystem in murine small intestine. Proc Natl Acad Sci U S A 113, E5934–E5943. [PubMed: 27638207]

Uhlen M, Fagerberg L, Hallstrom BM, Lindskog C, Oksvold P, Mardinoglu A, Sivertsson A, Kampf C, Sjostedt E, Asplund A, et al. (2015). Proteomics. Tissue-based map of the human proteome. Science 347, 1260419. [PubMed: 25613900]

VanDussen KL, Carulli AJ, Keeley TM, Patel SR, Puthoff BJ, Magness ST, Tran IT, Maillard I, Siebel C, Kolterud A, et al. (2012). Notch signaling modulates proliferation and differentiation of intestinal crypt base columnar stem cells. Development 139, 488–497. [PubMed: 22190634]

Wang B, Rong X, Palladino END, Wang J, Fogelman AM, Martin MG, Alrefai WA, Ford DA, and Tontonoz P (2018). Phospholipid Remodeling and Cholesterol Availability Regulate Intestinal Stemness and Tumorigenesis. Cell Stem Cell 22, 206–220 e204. [PubMed: 29395055]

Wang W, Ishibashi J, Trefely S, Shao M, Cowan AJ, Sakers A, Lim HW, O'Connor S, Doan MT, Cohen P, et al. (2019). A PRDM16-Driven Metabolic Signal from Adipocytes Regulates Precursor Cell Fate. Cell Metab 30, 174–189 e175. [PubMed: 31155495]

Wei P, Dove KK, Bensard C, Schell JC, and Rutter J (2018). The Force Is Strong with This One: Metabolism (Over)powers Stem Cell Fate. Trends Cell Biol 28, 551–559. [PubMed: 29555207]

Wellen KE, Hatzivassiliou G, Sachdeva UM, Bui TV, Cross JR, and Thompson CB (2009). ATP-citrate lyase links cellular metabolism to histone acetylation. Science 324, 1076–1080. [PubMed: 19461003]

Wong BW, Wang X, Zecchin A, Thienpont B, Cornelissen I, Kalucka J, Garcia-Caballero M, Missiaen R, Huang H, Bruning U, et al. (2017). The role of fatty acid beta-oxidation in lymphangiogenesis. Nature 542, 49–54. [PubMed: 28024299]

Yan KS, Chia LA, Li X, Ootani A, Su J, Lee JY, Su N, Luo Y, Heilshorn SC, Amieva MR, et al. (2012). The intestinal stem cell markers Bmi1 and Lgr5 identify two functionally distinct populations. Proc Natl Acad Sci U S A 109, 466–471. [PubMed: 22190486]

Yao CH, Liu GY, Wang R, Moon SH, Gross RW, and Patti GJ (2018). Identifying off-target effects of etomoxir reveals that carnitine palmitoyltransferase I is essential for cancer cell proliferation independent of beta-oxidation. PLoS Biol 16, e2003782. [PubMed: 29596410]

Zeng X, Jedrychowski MP, Chen Y, Serag S, Lavery GG, Gygi SP, and Spiegelman BM (2016). Lysine-specific demethylase 1 promotes brown adipose tissue thermogenesis via repressing glucocorticoid activation. Genes Dev 30, 1822–1836. [PubMed: 27566776]

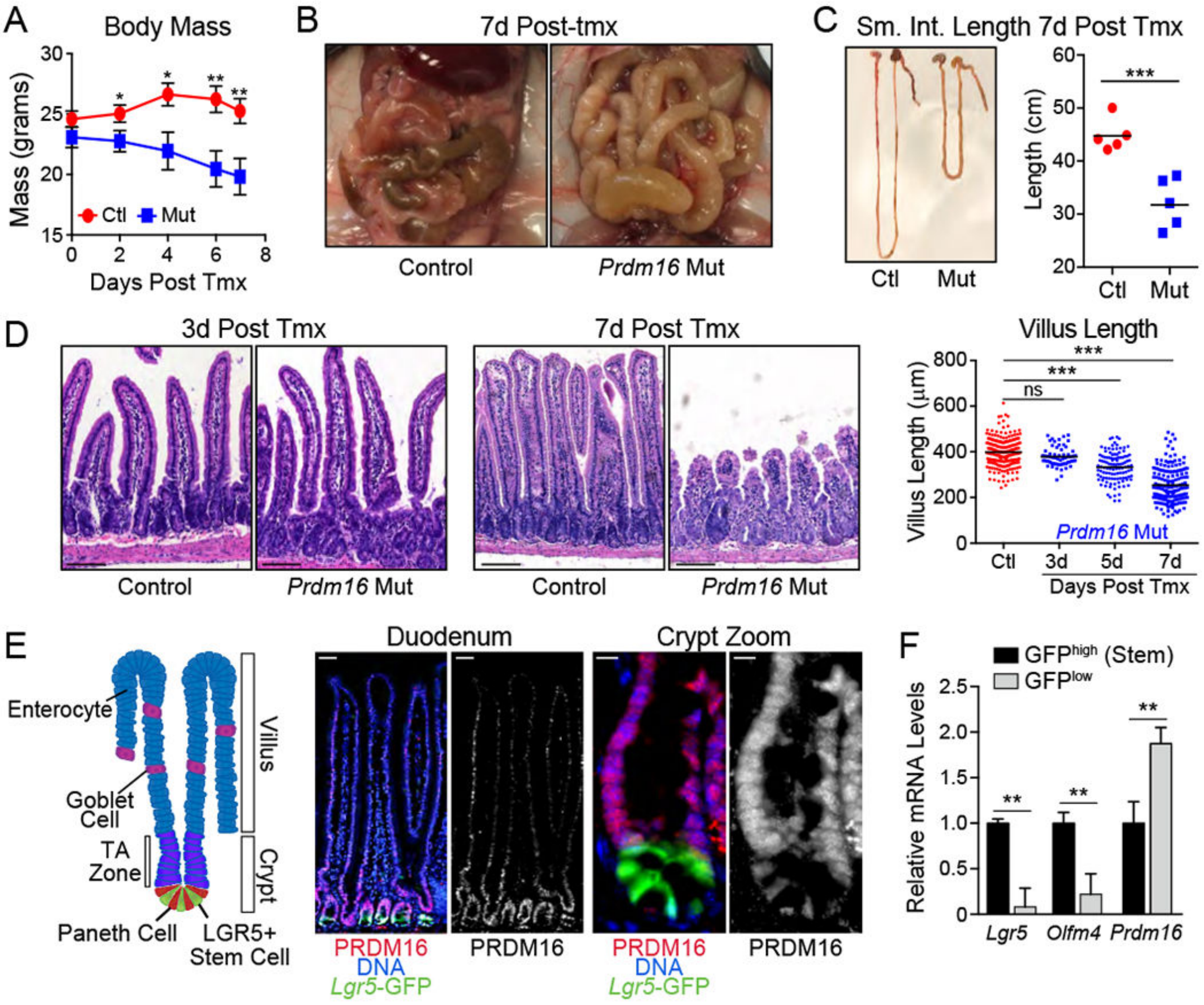

Figure 1: *Prdm16* is required for small intestine maintenance.

A-D) Phenotypes of Control (*Prdm16*$^{loxP/loxP}$) and *Prdm16* mutant (*R26R*^{CreERT2}; *Prdm16*$^{loxP/loxP}$) animals after injection with tmx. A) Body mass following tmx injection. n=4 mice/group. B) Gross appearance of small intestines at 7d post tmx. C) Small intestine length at 7d post tmx. D) Hematoxylin/eosin histology of duodenum at 3d and 7d post tmx (left) with quantification of villus length at 3d, 5d, and 7d (right). n=4 mice/group.

E) (left) Schematic of intestinal villus/crypt structure and cell identities. TA Zone=Transit Amplifying Zone. (center, right) Duodenal sections stained for PRDM16 (red) and *Lgr5*-GFP (green). full villus (center), crypt compartment (right). DNA: DAPI, blue. Sub-panels: [left, overlay] [right] PRDM16 alone (white).

F) mRNA levels of *Prdm16* and stem cell markers in FACS isolated *Lgr5*^{GFP}-low or -high epithelial cells from duodenal crypts. n=3 mice.

All panels show mean ± SEM, *p<0.05, **p<0.01, ***p<0.001. Scale Bars: 100 µm (D,E Left), 10 µm (E Right).

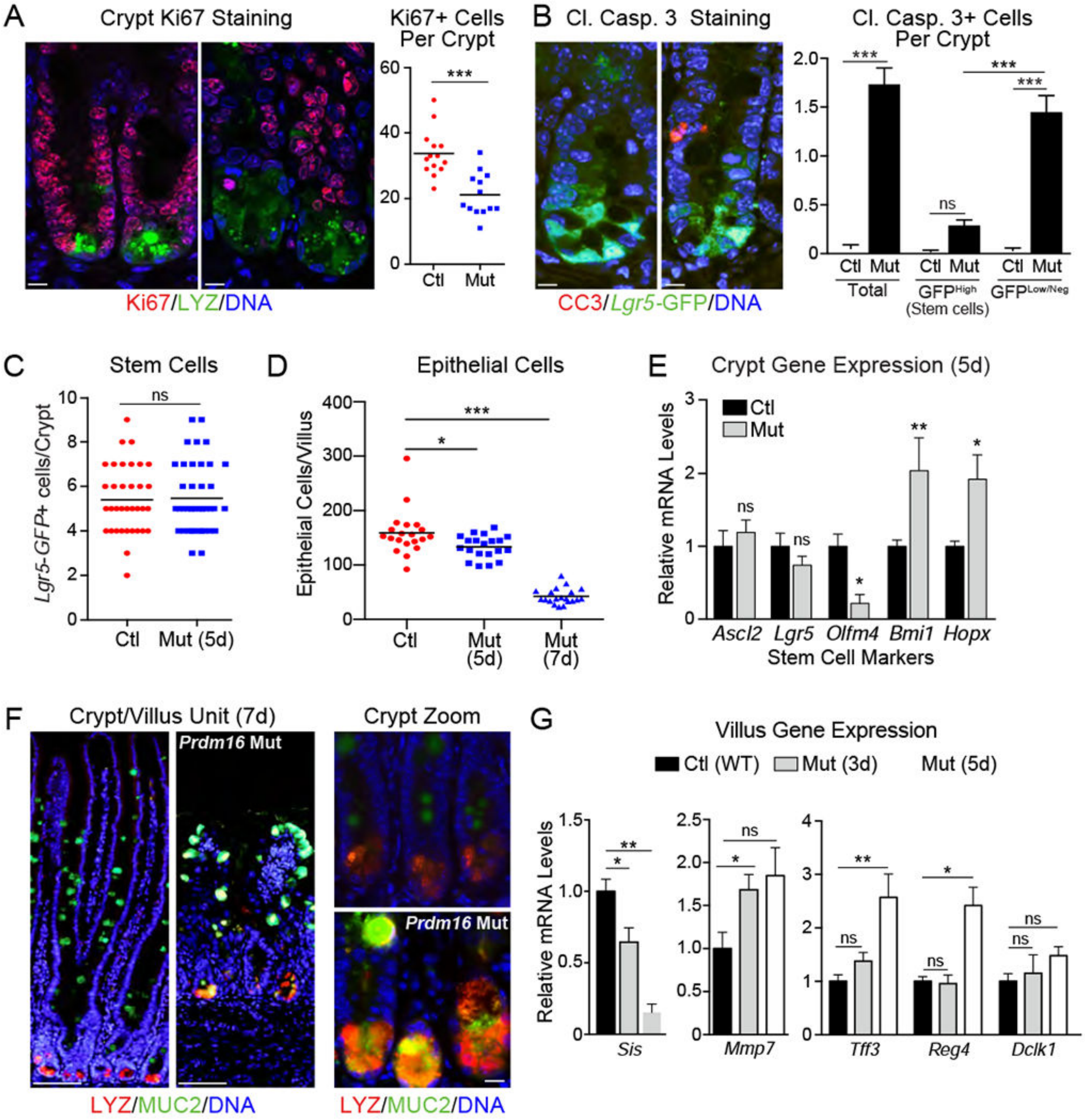

Figure 2: *Prdm16* deletion induces crypt apoptosis and disrupts cell type composition.

A) (left) Immunofluorescence staining of Ki67+ (red) proliferative cells in crypts of Control (*Prdm16*$^{loxP/loxP}$) and *Prdm16* mutant (*R26R*^{CreERT2}; *Prdm16*$^{loxP/loxP}$) mice 5d after tmx injection. Lysozyme (LYZ; green), DNA (DAPI, blue). (right) Quantification of Ki67+ cells/crypt. n=13 to 14 crypts, 3 mice per group.

B) (left) Immunofluorescence staining of Cleaved Caspase 3 (CC3; red) in duodenal crypts from Control (corn oil-treated) and *Prdm16* mutant (Mut; tmx-treated) *R26R*^{CreERT2}; *Lgr5*$^{GFP/CreERT2}$; *Prdm16*$^{loxP/loxP}$ mice (at 5d). *Lgr5*-GFP (green), DNA (DAPI, blue).

(right) Quantification of CC3+ stem (GFP^{hi}) or TA (GFP$^{low/neg}$) cells. n=88-91 crypts from 3 mice.

C) Quantification of *Lgr5*-GFP+ stem cells in mice from (B). n=35-41 crypts from 3 mice.

D-G) Control (*Prdm16*$^{loxP/loxP}$) and *Prdm16* mutant (*R26R*^{CreERT2}; *Prdm16*$^{loxP/loxP}$) (Mut) mice were injected with tmx. **D)** Counts of epithelial cells/villus at 5d and 7d post tmx. n=20 villi from 3 mice. **E)** mRNA levels of stem cell markers in isolated crypts 5d post tmx. n=5-7 mice. **F)** Immunofluorescence in villi and crypts at 7d post tmx. Full villus (left), magnified crypt (right). Goblet cell marker (Mucin 2; MUC2, green), Paneth cell marker (Lysozyme; LYZ, red), DNA (DAPI, blue). arrowheads = MUC2/LYZ double-positive cells. **G)** mRNA levels of absorptive (left) and secretory cell (right) markers in isolated villi or crypts (for *Mmp7)* at 3d and 5d post tmx. n= 4-7 mice.

All panels show mean ± SEM, *p<0.05, **p<0.01, ***p<0.001. Scale bars: 10 μm (A,B, F right); 100 μm (F left).

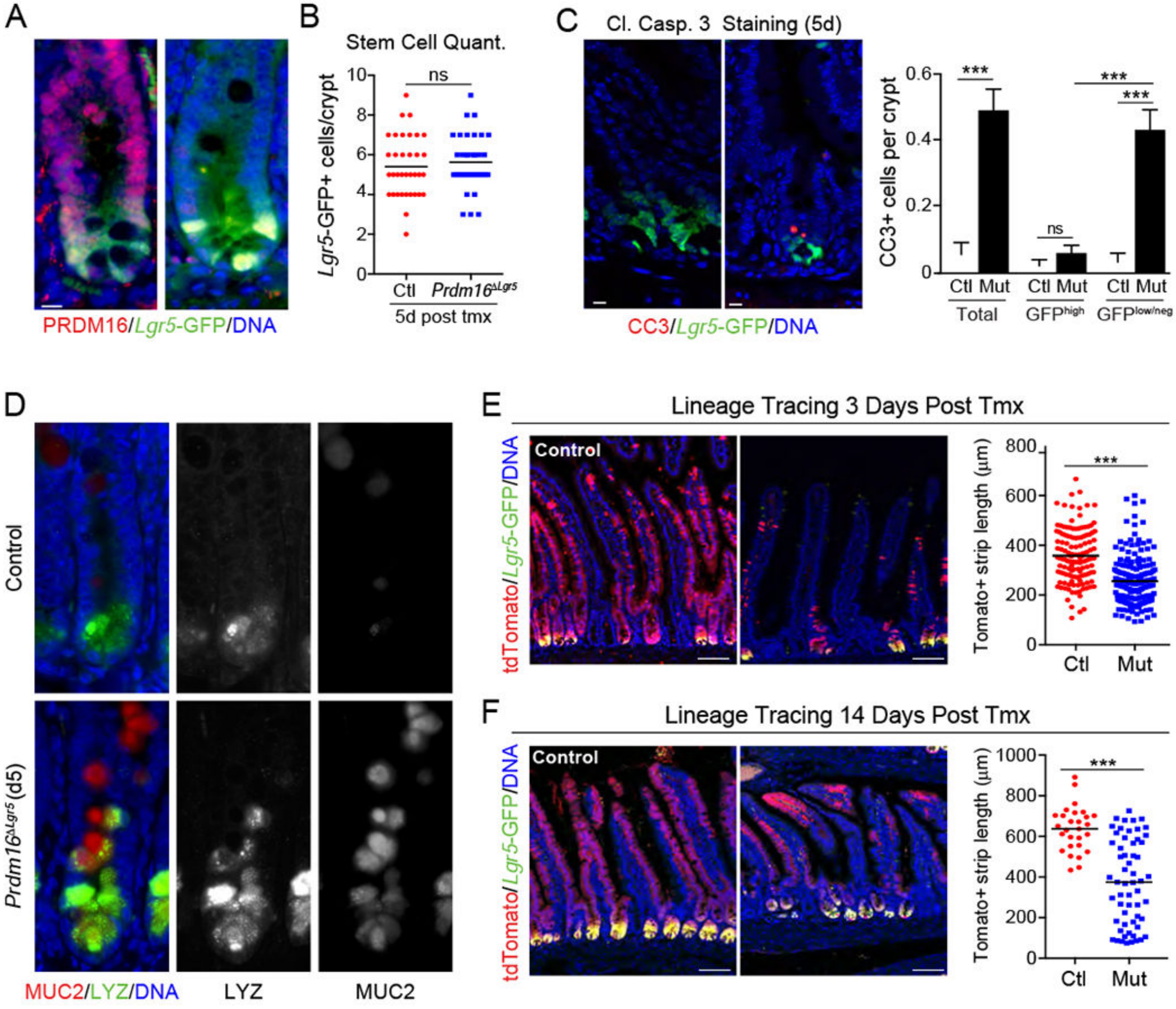

Figure 3: Loss of *Prdm16* in stem cells leads to TA cell apoptosis and diminished epithelial differentiation

A-D) *Lgr5*$^{GFP/Cre\text{-}ERT2}$;*Prdm16*$^{loxP/loxP}$ mice were treated with tmx (mutant; *Prdm16*$^{\Delta Lgr5}$) or vehicle (corn oil; Control). **A)** Immunostaining of PRDM16 (red) and *Lgr5*-GFP (green) in duodenal crypts at 7d post tmx. DNA (DAPI, blue). **B)** Quantification of *Lgr5*$^{GFP+}$ stem cells per crypt at 5d. n=35 crypts from 3 mice. **C)** (left) Duodenal crypts stained for cleaved Caspase 3 (CC3; red) at 5d. (right) Quantification of CC3+ stem (GFP^{hi}) or TA (GFP$^{low/neg}$) cells using an intensity threshold (Thermal LUT in Image J). Controls were shared with experiment in Figure 2B. n=91-188 crypts from 3 mice per group. **D)** Immunostaining of Mucin2 (MUC2; red) and Lysozyme (LYZ; green) in duodenal crypts at 5d. Arrowheads indicate MUC2/LYZ double-positive cells. n=3 mice.

E-F) Lineage tracing of *Lgr5*+ stem cell progeny in Control (*Prdm16*$^{loxP/+}$) and *Prdm16* mutant (*Prdm16*$^{loxP/oxP}$; *Prdm16*$^{\Delta Lgr5}$) reporter mice (*Lgr5*$^{GFP/Cre\text{-}ERT2}$;*R26R*$^{lox\text{-}stop\text{-}lox\text{-}tdTomato}$). Marked epithelial strip length was measured for continuous streaks of tdTomato+ (Red) epithelial cells ascending the villi at: **E)** 3d [n=132-190 villi from 3 mice] or **F)** 14d [n=28-58 villi from 3 mice] post tmx. *Lgr5*-GFP (green), DNA (DAPI, blue).

All panels show mean ± SEM, *p<0.05, **p<0.01, ***p<0.001. Scale bars: 10 µm (A, C, ; (D) 100 µm (E, F).

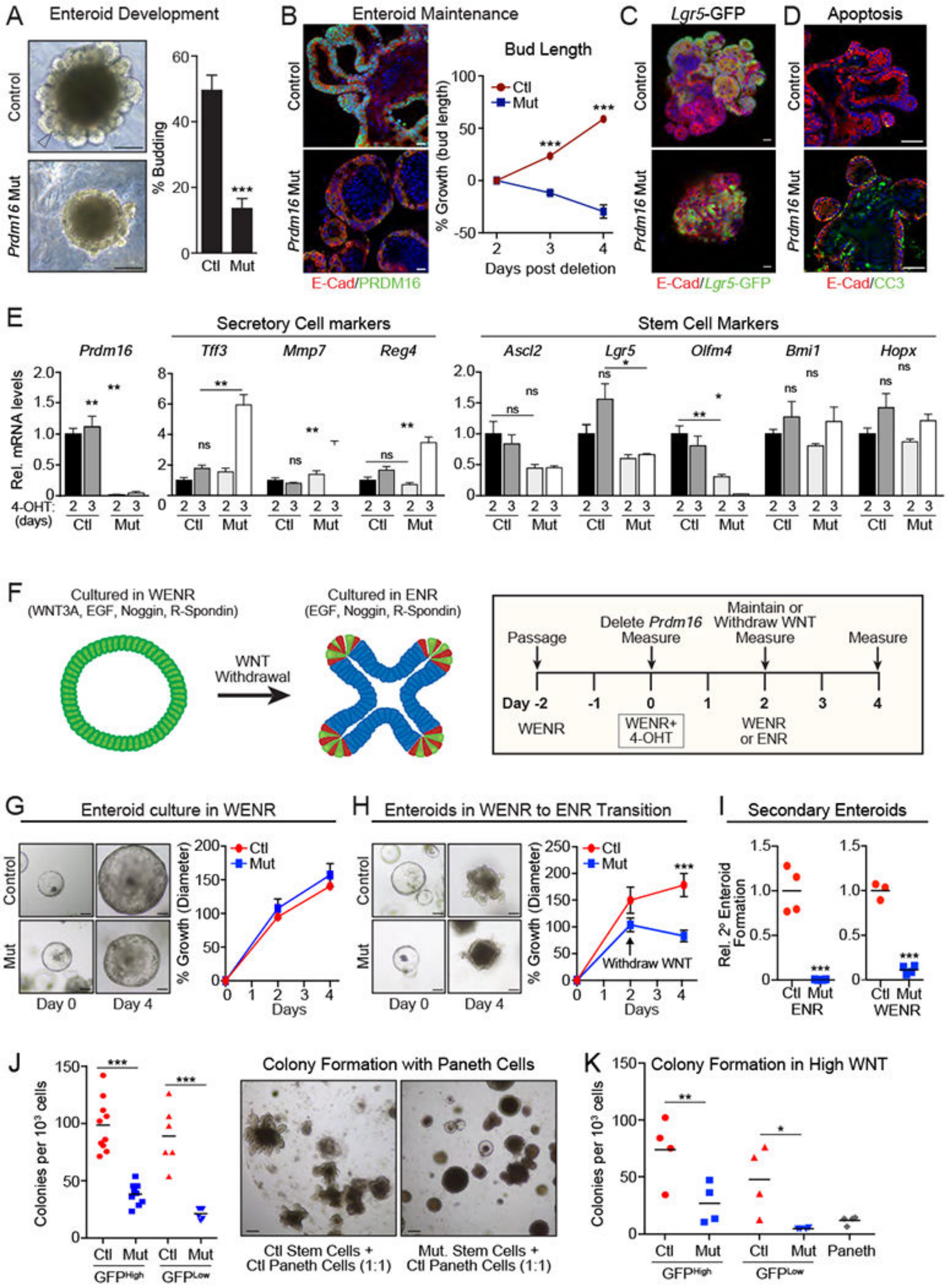

Figure 4: *Prdm16* is required for the development and maintenance of duodenal enteroids.

(A) Images and quantification of budding (defined as one or more bud) in Control (*Prdm16*$^{loxP/loxP}$) and *Prdm16* mutant (*R26R*$^{Cre\text{-}ERT2}$;*Prdm16*$^{loxP/loxP}$) duodenal enteroids grown in ENR, 3d following 4-OHT treatment. Arrowhead shows bud. n=410-554 enteroids. **B)** Growth or regression of buds following 4-OHT treatment of mature budded enteroids. *%* growth = change in bud length / initial bud length for n=7-8 enteroids. PRDM16 (green), E-Cadherin (red), DNA (DAPI, blue).

C) Immunostaining of *Lgr5*-GFP+ (green) stem cells in control and *Prdm16*-mutant enteroids, 4d after inducing deletion. Enteroids were from *Lgr5*$^{GPP/CreERT2}$; *Prdm16*$^{loxP/loxP}$ (control) or *R26R*^{CreERT2}; *Lgr5*$^{GFP/CreERT2}$; *Prdm16*$^{loxP/loxP}$ (Mut) mice and treated with vehicle (control) or 4-OHT (Mut). E-Cadherin (red), DNA (DAPI, blue).

D) Cleaved Caspase 3 (CC3+) apoptotic cells (green) in control (*Prdm16*$^{loxP/loxP}$) and *Prdm16* mutant (*R26R*$^{Cre\text{-}ERT2}$;*Prdm16*$^{loxP/loxP}$) duodenal enteroids 3d after treatment with 4-OHT. E-Cadherin (red), DNA (DAPI, blue).

E) mRNA levels of cell type-specific marker genes in control and *Prdm16* mutant enteroids at 2d and 3d post 4-OHT treatment. n=4.

F-I) Control and *Prdm16* mutant enteroids were established in Wnt^{high} medium (WENR), prior to treatment with 4-OHT to delete *Prdm16*. **F)** Schematic of experimental protocol. **G)** Enteroid growth in WENR. n=11-13 enteroids. % growth = mean change in diameter / initial diameter. **H)** Enteroid growth during transfer from WENR to ENR medium. n=16-23 enteroids. **I)** Secondary enteroids formed per well from passaged fragments of Control or *Prdm16* mutant enteroids cultured in WENR or ENR medium. n=3-4 wells.

J-K) Colony formation efficiency of GFP^{hi} and GFP^{low} cells isolated by FACS from control (*Lgr5*$^{GFP/Cre\text{-}ERT2}$; *Prdm16*$^{loxP/+}$) or *Prdm16* mutant (*R26R*^{CreERT2}; *Lgr5*$^{GFP/CreERT2}$; *Prdm16*$^{loxP/loxP}$) mice 3d after *in vivo* tamoxifen injection, when co-cultured with control Paneth Cells (J; n=10 wells) or in high WNT conditions (K; n=4 wells).

All panels show mean ± SEM, *p<0.05, **p<0.01, ***p<0.001. Scale bars: 100 μm (A, G, H, J); 20 μm (B); 50 μm (C,D).

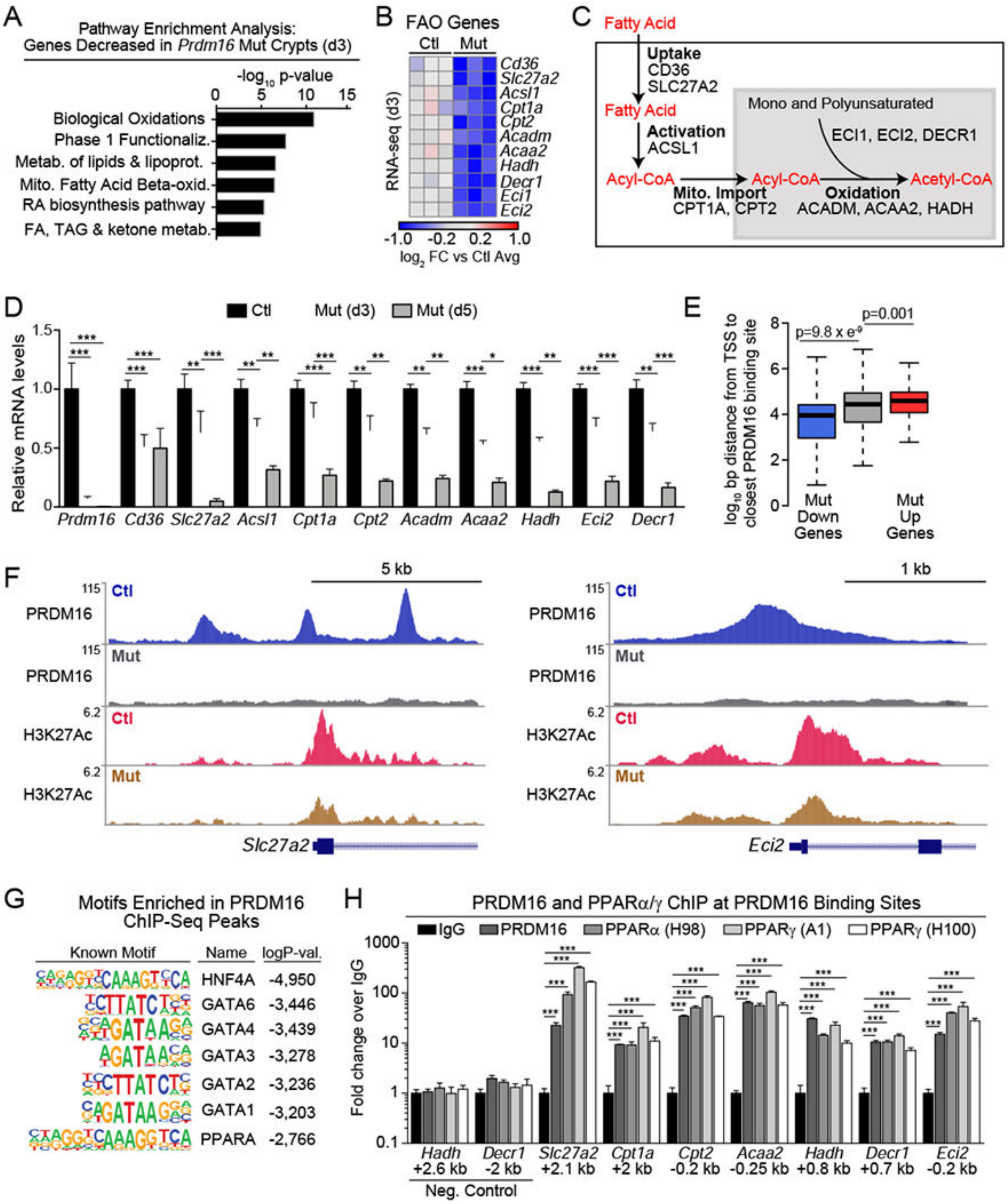

Figure 5: PRDM16 binds and promotes the expression of fatty acid oxidation genes

A-B) RNA-seq analysis of isolated duodenal crypts from *Prdm16*$^{loxP/loxP}$ (control) or *R26R*$^{Cre-ERT2}$;*Prdm16*$^{loxP/loxP}$ (mutant) animals at 3d after tmx injection. **A)** Pathway analysis of down-regulated genes (FDR<0.05) in mutant crypts. **B)** Downregulated FAO genes meeting a threshold of FDR<0.1 are displayed in a heat map of $\log_2$ fold-change (FC) relative to mean expression in controls. n=3 mice per group.

C) Schematic of key steps of FAO to acetyl-CoA generation with associated enzymes.

D) mRNA levels of FAO genes in control and *Prdm16* mutant crypts at 3d and 5d after tmx injection. n=4 (control/mutant d3), n=5 (mutant d5).

E) Distance of PRDM16 ChIP-Seq peaks from the transcriptional start site (TSS) of downregulated (blue), unchanged (gray), or upregulated (red) genes in *Prdm16*-mutant crypts by RNA-seq at 3d post tmx.

F) ChIP-seq tracks for PRDM16 and H3K27Ac at FAO genes *Slc27a2* and *Eci2* in control and mutant duodenal crypts.

G) Transcription factor binding motifs enriched at PRDM16 ChIP-seq peaks.

H) CHIP-qPCR analysis of PRDM16, PPARα and PPARγ (two antibodies) binding at PRDM16-ChIP-seq binding regions near FAO gene promoters in duodenal crypts. Negative control sites are ~3 kb from PRDM16 peaks. Distance from TSS is shown in kilobases (kb), fold-change shown relative to normal-IgG control ChIP. n=3 biological ChIP replicates. Panels (D,H) show mean ± SEM, *p<0.05, **p<0.01, ***p<0.001.

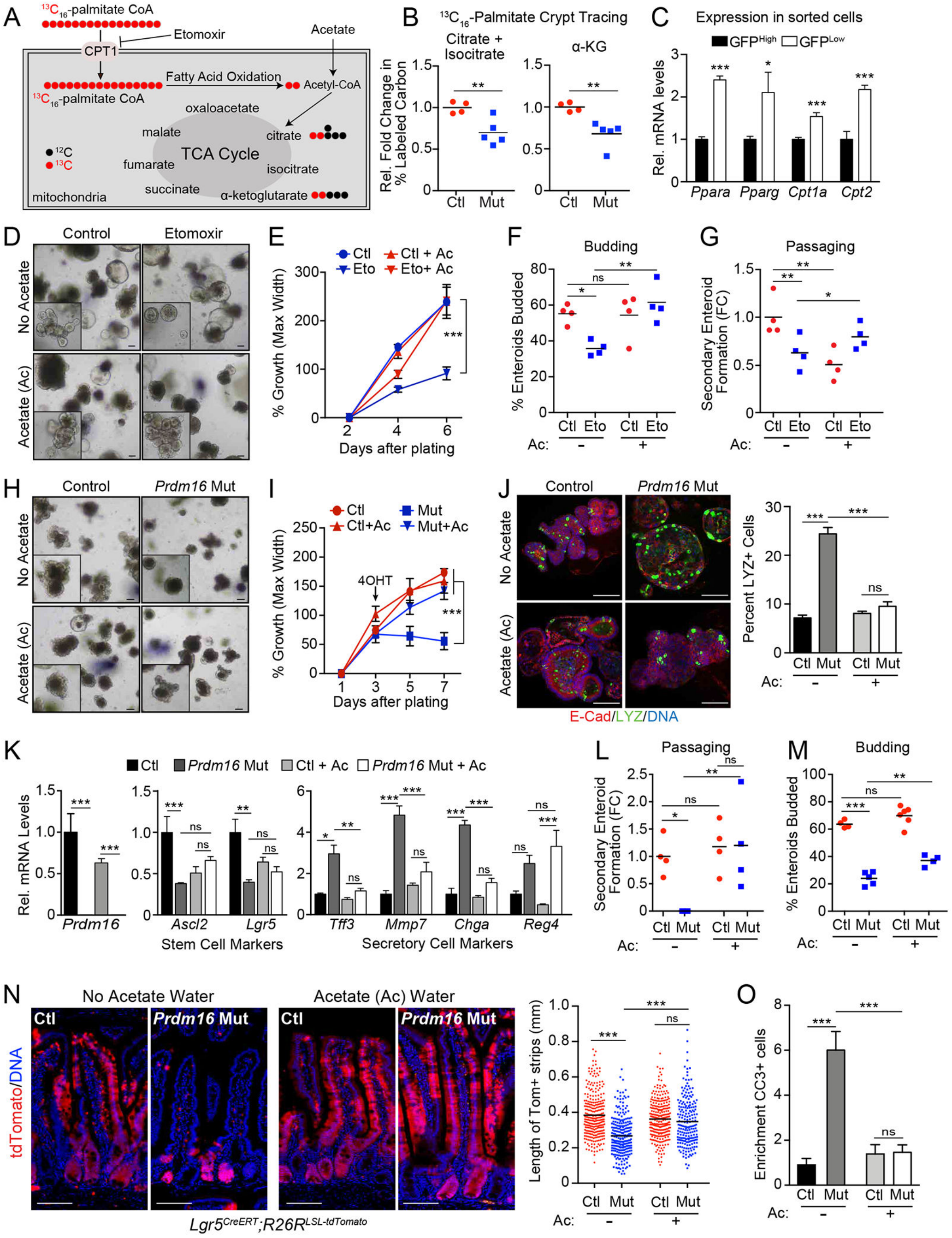

Figure 6: PRDM16 regulates intestinal growth and maintenance by promoting FAO.

A-B) Mass spectrometry analysis of $^{13}C_{16}$-palmitate incorporation into TCA cycle metabolites. A) schematic. B) Relative ^{13}C-labeling of the citrate/isocitrate and α-ketoglutarate pools in control (*Prdm16*$^{loxP/loxP}$) vs. *Prdm16* mutant (*R26R*^{CreERT2}; *Prdm16*$^{loxP/loxP}$) crypts isolated 3d after tmx injection. ^{13}C-labeling = Σ (% of isotopomer multiplied by labeled carbons in isotopomer) divided by the number of carbons in molecule. n=4-5 mice per group.

C) mRNA levels of indicated FAO genes in FACS-isolated *Lgr5*-GFP$^{\text{Hi}}$ or *Lgr5*-GFP$^{\text{low}}$ epithelial cells from the duodenum of *Lgr5*$^{GPP/Cre\text{-}ERT2}$ mice. n=3 mice.

D-G) Wildtype enteroids (in ENR medium) were treated with: (1) vehicle or etomoxir, and (2) sodium chloride (No Acetate) or Acetate (Ac). **D)** Brightfield images with magnified inset. **E)** Quantification of enteroid growth. n=32-41 enteroids. **F)** Quantification of enteroid budding (one or more buds). n=4 wells. **G)** Secondary enteroid formation from fragments of passaged enteroids. n=4 wells. Etomoxir (Eto), 50 μM in water; NaAc/NaCl, 5 mM in water. Enteroids were treated with NaAc / NaCl for 2d before addition of Eto treatment.

H-N) Control or *Prdm16* mutant enteroids (in ENR medium) were treated with 5mM sodium acetate (Ac) or 5mM sodium chloride (No Acetate). **H)** Brightfield images with magnified insets. **I)** Enteroid growth. n=16-21 enteroids. **J)** Immunostaining of Lysozyme-positive (green) Paneth cells in control and *Prdm16*-mutant enteroids, 4d after inducing deletion. Enteroids were from *Prdm16*$^{loxP/loxP}$ (control) or *R26R*^{CreERT2}; *Prdm16*$^{loxP/loxP}$ (Mut) mice and treated with 4-OHT with additional treatment of acetate or no acetate treatment (NaCl, 5mM). E-Cadherin (red), DNA (DAPI, blue). Percentage of enteroid cells positive for Lysozyme staining are quantified in the graph. **K)** mRNA levels of cell type-specific marker genes in control and *Prdm16* mutant enteroids at 4days post 4-OHT treatment with or without acetate treatment. n=4. **L)** Secondary enteroid formation from fragments of passaged enteroids. **M)** Enteroid budding (defined as one or more bud). n=4-6 wells. n=4 wells; NaAc/NaCl, 5 mM in water. Enteroids were pretreated with NaAc / NaCl for 2d after plating but before treatment with 4-OHT.

N) Lineage tracing of stem cell progeny in *Prdm16*$^{loxP/+}$ (control) *or Prdm16*$^{loxP/loxP}$ (mutant) tdTomato reporter mice. Animals received drinking water containing either 150 mM NaAc (Ac) or NaCl (No Acetate) 2d before tmx treatment. Length of marked villus epithelial cell strips was measured for continuous strips of Tomato+ (red) epithelial cells ascending the villi at 4d post tmx treatment. n=200-291 villi measured from >=4 mice per group. tdTomato (red), DNA (DAPI, blue). **O)** Quantification of Cleaved caspase-3 positive cells per tdTomato positive crypt relative to the number of cleaved caspase-3 positive cells in tdTomato negative crypts. N=303-423 crypts from 3 or more mice per group.

All panels show mean ± SEM, *p<0.05, **p<0.01, ***p<0.001. Scale bars: 100 μm (D, H, J); 50 μm (N).

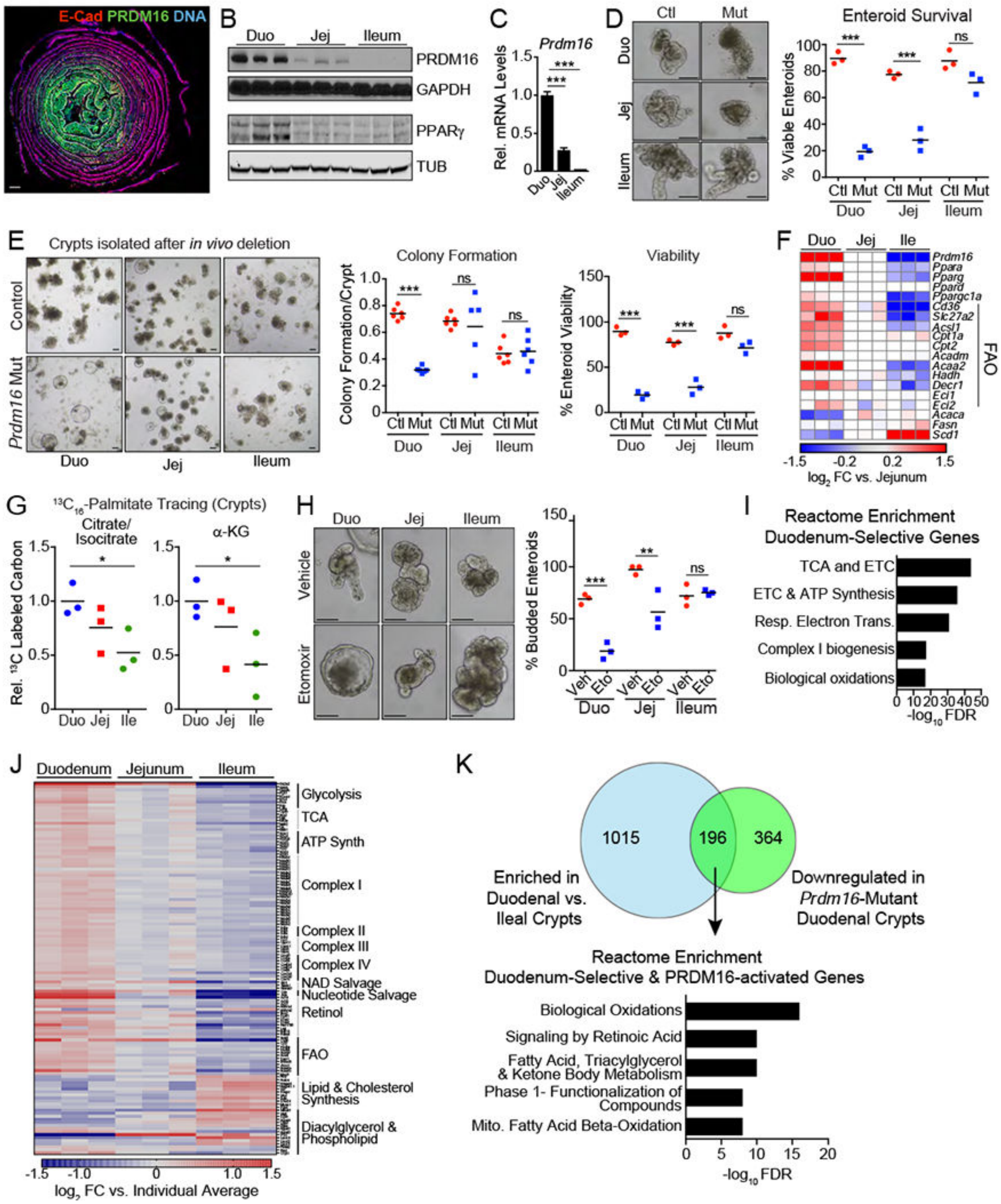

Figure 7: PRDM16-driven FAO selectively regulates the development and maintenance of upper intestinal enteroids

A) "Swiss roll" immunostaining of PRDM16 (green) in small intestine, with duodenum at the center and ileum at the periphery. E-cadherin (red), DNA (DAPI, blue). Panel is stitched composite of 10X images.

B) Western blot analysis of PRDM16 and PPARγ expression in duodenal, jejunal, and ileal crypts. Loading controls are GAPDH and α-Tubulin (TUB). n=3 mice.

C) mRNA levels of *Prdm16* in duodenal, jejunal, and ileal crypts. n=3 mice.

D) (left) Control (*Prdm16*$^{loxP/loxP}$) and *Prdm16* mutant (*R26R*^{CreERT2}; *Prdm16*$^{loxP/loxP}$) enteroids derived from duodenal, jejunal, and ileal crypts. Enteroids were analyzed 7d post 4-OHT treatment. (right) Quantification of viable enteroids. n=54-121 enteroids, n=3 wells.

E) Enteroid formation from duodenal, ileal, and jejunal crypts of control (*Prdm16*$^{loxP/loxP}$) and *Prdm16* mutant (*R26R*^{CreERT2}; *Prdm16*$^{loxP/loxP}$) mice 3d after tmx injection. Colony formation and viability were assessed 2d and 7d after plating, respectively.

F) Expression heat map of *Prdm16, Ppar* isoforms, FAO, and fatty acid synthesis genes, as measured by qRT-PCR. n=3 mice.

G) Mass spectrometry analysis of relative ^{13}C-labeling of the citrate/isocitrate and α-ketoglutarate pools in duodenal, jejunal, and ileal crypts after a 90-minute incubation in $^{13}C_{16}$-palmitate (relative to duodenum). ^{13}C-labeling = Σ (% of isotopomer multiplied by labeled carbons in isotopomer) divided by the number of carbons in molecule. n=3 mice.

H) Quantification of budding (one or more buds) in duodenal, jejunal, and ileal enteroids following treatment with vehicle or etomoxir (Eto; 50 μM). n=79-239 from 4 wells.

I-K) RNA-seq analysis of wildtype crypts from duodenum, jejunum, and ileum. n=3. **I)** Reactome enrichment analysis of genes with selective expression in duodenal vs. ileal crypts. **J)** Expression heat map of a curated set of metabolism genes showing relative regional expression. Scale is log2 fold change versus average expression across crypts for each individual replicate. **K)** Venn diagram of overlap between duodenal crypt-enriched genes and genes downregulated in *Prdm16* mutant crypts (top). Intersecting gene set was used for Reactome enrichment analysis (bottom).

All panels show mean ± SEM, $^{*}p<0.05$, $^{**}p<0.01$, $^{***}p<0.001$. Scale bars: 1 mm (A), 100 μm (D, E, H). Duo= duodenal, Jej=jejunal, Ile=ileal. Ctl= Control. Veh=vehicle.

KEY RESOURCES TABLE

REAGENT or RESOURCE	**SOURCE**	**IDENTIFIER**
Antibodies		
Rb anti Cleaved Notch1 (Val1744) (D3B8)	Cell Signaling	RRID:AB_2153348
Rb anti Cleaved Caspase 3 (Asp175) (5A1E)	Cell Signaling	RRID: AB_2070042
Ms anti E-Cadherin	BD Transduction	RRID:AB_397580
Rb anti KI67 (SP6)	Abcam	RRID:AB_302459
Gt anti Lysozyme C Antibody (W-20)	Santa Cruz	RRID:AB_2138793 (Disc)
Rb anti Muc2 (H-300)	Santa Cruz	RRID:AB_2146667 (Disc)
Ms anti-p53 (1C12)	Cell Signaling	RRID:AB_331743
Gt anti GFP	Abcam	RRID:AB_305643
Rb anti Prdm16	P. Seale	Made in house
Rb anti Prdm16	R and D	RRID:AB_10717965
Ms anti GAPDH (GA1R)	Thermo	RRID:AB_10977387
Ms anti Tubulin (DM1A)	Sigma	RRID:AB_477583
Rb anti Pparg (H-100)	Santa Cruz	RRID:AB_654710
Rb anti Pparg (81B8)	Cell Signaling	RRID:AB_823598
Rb anti Ppara (H-98)	Santa Cruz	RRID:AB_2165737
Rb anti Lysozyme C	Agilent	RRID:AB_2341230
Rb anti Chromogranin A	Abcam	RRID:AB_301704
Rb anti MUC2	Cloud Clone	RRID:AB_2811028
Rb anti RFP	Rockland	RRID:AB_2209751
Ms anti IFNAR1 (MAR15A3)	Leinco Tech. Inc	RRID:AB_2491621
anti-rabbit IgG, Alexa 647 donkey	Thermo Fisher	RRID:AB_2536183
anti-goat IgG, Alexa 488 donkey	Thermo Fisher	RRID:AB_2534102
anti-mouse IgG, Alexa 555 donkey	Thermo Fisher	RRID:AB_2536180
anti-rabbit Alexa 488 goat	Thermo Fisher	RRID:AB_2536180
DAPI	Roche	Cat#10236276001
anti- CD117 (c-Kit) APC/Cy7 (2B8)	Biolegend	RRID:AB_1626280
anti-CD24 Pacific Blue (MI/69)	Biolegend	RRID:AB_572011
anti-CD31 PE (390)	Biolegend	RRID:AB_312902
anti-CD45 PE (30-F11)	Biolegend	RRID:AB_312971
anti-Ter119 PE (Ly 76)	Biolegend	RRID:AB_313708
anti-CD326 (EpCAM) APC (G8.8)	EBioscience	RRID:AB_2734965
Anti-mouse IgG IR Dye 680RD	Li-Cor	RRID:AB_10953628
and anti-rabbit IgG IRDye 800CW	Li-Cor	RRID:AB_621848
anti-rabbit-IgG-HRP	Cell Signaling	RRID:AB_2099233
anti-mouse IgG (H/L)-HRP	Cell Signaling	RRID:AB_330924
Anti-H3K27ac	Active Motif	RRID:AB_2561016

REAGENT or RESOURCE	**SOURCE**	**IDENTIFIER**
Normal Rabbit IgG	Cell Signaling	RRID:AB_1031062
Chemicals, Peptides, and Recombinant Proteins		
Intesticult	Stem Cell Tech.	Cat#06005
Murine EGF, Recombinant	Preprotech	Cat#315-09
Murine Noggin, Recombinant	Preprotech	Cat#250-38
Human R-Spondin-1, Recombinant	Preprotech	Cat#120-38
Human Wnt3a, Recombinant	R&D Systems	Cat#5036-WN-010
HBSS, No Ca+, No Mg+	Thermo Fisher	Cat#14175079
EDTA (Disodium Salt)	Fisher	Cat#BP 120-500
CHIR 99021	Biovision	Cat#1677-5
N-Acetyl-L-cysteine	Sigma	Cat#A9165
Y-27632	Cell Signaling	Cat#13624S
N2 Supplement	Thermo Fisher	Cat#17502048
B-27 Supplement	Thermo Fisher	Cat#17504044
Advanced DMEM F12 Medium	Thermo Fisher	Cat#12634010
Matrigel	Corning	Cat#356231
Nicotinamide	Sigma	Cat#N0636
RPMI 1640	Invitrogen	Cat#11835030
L-Carnitine	Sigma	Cat#C0283
L-Glutathione, Reduced	Sigma	Cat#G4251
Dulbecco’s MEM (DMEM) F-12, w/o Amino Acids, L-Glutamine, Glucose, Sodium Pyruvate	US Biologicals	Cat#D9807-11
Glutamax 100x	Thermo Fisher	Cat#35050061
Hepes 1M	Thermo Fisher	Cat#15630080
MEM non-essential amino acids, 100x	Thermo Fisher	Cat#11140050
MEM Amino Acids Solution, 50X	Thermo Fisher	Cat#11130051
D-Glucose (U-13C6, 99%)	Cambridge Isotopes	Cat#CLM-1396
Palmitic Acid ($^{13}C_{16}$, 99%)	Cambridge Isotopes	Cat# CLM-3957
Palmitic Acid	Sigma	Cat#76119
TrypLE Express	Invitrogen	Cat#12605010
Tamoxifen (Free Base)	Sigma	Cat#T5648
4-hydroxy-tamoxifen	Sigma	Cat#H6278
Etomoxir	Sigma	Cat#E1905
Corn Oil	Sigma	Cat#C8267
16% Paraformaldehyde	EMS	Cat#15710
Normal Donkey Serum	Sigma	Cat#D9663
Vectashield	Vector Biolabs	Cat#H-1000
Protein-A Sepharose CL-4B Beads	GE Healthcare	Cat#17-0780-01
Acetonitrile (HPLC)	Fisher	Cat#A998-1

REAGENT or RESOURCE	**SOURCE**	**IDENTIFIER**
Methanol (HPLC)	VWR	Cat#MX0475-1
Water (HPLC)	Fisher Chemical	Cat#W5-1
Formic Acid LC/MS Grade	Pierce	Cat#28905
Fluoroscein isothiocyanate (FITC) dextran	Sigma	Cat#FD4
Blood Agar (TSA w/5% Sheep Blood)	Fisher	Cat#R01201
TruSeq RNA Sample Prep Kit v2 set A	Illumina	Cat#RS-122-2001
PCR Master Mix, Power SYBR Green	Applied Biosystems	Cat#4367659
MILLIPLEX Mouse Cytokine/Chemokine Magnetic Bead Immunology Multiplex Assay	Millipore	Cat#MCYTMAG-70K-PX32
Lipofectamine 2000	Invitrogen	Cat#11668027
PEG-It	System Bioscience	Cat#LV810A-1
NEBNext Ultra II DNA Library Prep with Sample Purification Beads	NEB	Cat#E7103
NEB Next Ultra RNA Library Prep Kit	NEB	Cat#E7530
Sodium Acetate	Sigma	Cat#S5636
Sodium Chloride	Sigma	Cat#S9888
DNase I, RNase Free, Recombinant	Roche	Cat#04716728001
DMEM	MediaTech	Cat#MT10-017-CV
DTT	Roche	Cat#3117006007
Red Blood Cell Lysis Buffer	Biolegend	Cat#420301
Dispase II	Roche	Cat#4942078001
Fetal Bovine Serum (Lot 401714)	Omega Scientific	Cat#FB-11
Fluorobrite DMEM	Gibco	Cat#A18967
AbC Total Compensation Beads	Molecular Probes	Cat#A10497
7-AAD Viability Dye	Biolegend	Cat#420404
Arcturus PicoPure RNA Isolation Kit	ThermoFisher	Cat#KIT0204
TRIzol	Invitrogen	Cat#15596018
Purelink RNA Mini columns	Invitrogen	Cat#LT-12183018
SuperSignal West Dura ECL	Fisher	Cat#PIA34075
HyBlot CL Autoradiography Film	Denville	Cat#E3012
ABI High-Capacity cDNA Synthesis kit	Applied Biosystems	Cat#4368813
Borg Decloaker RTU	Biocare	Cat#BD1000
TSA TMR Tyramide Reagent Pack	Akoya Biosciences	Cat#NEL742001KT
TSA Fluorescein Tyramide Reagent Pack	Akoya Biosciences	Cat#NEL741001KT
Bulls Eye Decloaking Buffer	Biocare	Cat#BULL1000 MX
GW9662	Sigma	Cat#M6191
GW6471	Sigma	Cat#G5045
Deposited Data		
RNA sequencing data	GEO repository	GSE121014
H3K27Ac ChIP Sequencing data	GEO repository	GSE121014

REAGENT or RESOURCE	SOURCE	IDENTIFIER
PRDM16 ChIP Sequencing	GEO repository	GSE121014
Experimental Models: Organisms/Strains		
R26CreER	The Jackson Laboratory	RRID:IMSR_JAX:004847
Lgr5-EGFP-IRES-creERT2	The Jackson Laboratory	RRID:IMSR_JAX:008875
Prdm16 loxP/loxP	Dr. Patrick Seale	RRID:IMSR_JAX:024992
Rosa26 loxp-stop-loxp tdTomato Reporter	The Jackson Laboratory	RRID:IMSR_JAX:007914
p53 loxP/loxP	The Jackson Laboratory	RRID:IMSR_JAX:008462
Oligonucleotides		
See Table S3 for Primers for Real-time PCR	Integrated DNA Technologies (IDT)	NA
Recombinant DNA		
PLKO.1-shRNA-Scramble	Addgene	RRID:Addgene_1864
PLKO.1-shRNA-Prdm16 2 (Sequence in table)	The RNAi Consortium (TRC)-Broad Institute via UPenn High-Throughput Screening Core	TRCN0000075460
PLKO.1-shRNA-Prdm16 1 (Sequence in table)	The RNAi Consortium (TRC)-Broad Institute via UPenn High-Throughput Screening Core	TRCN0000075458
pMD2.G	Addgene (D. Trono)	RRID:Addgene_12259
psPAX2	Addgene (D. Trono)	RRID:Addgene_12260
Software and Algorithms		
GraphPad Prism 7	Graphpad (https://www.graphpad.com/scientific-software/prism/)	RRID:SCR_002798
UCSC Genome Browser	UCSC (http://genome.ucsc.edu/)	RRID:SCR_005780
Human Protein Atlas (Human Prdm16 expression)	www.proteinatlas.org	RRID:SCR_006710
Morpheus (Heat Maps) by the Broad Institute	https://software.broadinstitute.org/morpheus/	RRID:SCR_017386
Homer	http://homer.ucsd.edu/	RRID:SCR_010881
Star Aligner	https://github.com/alexdobin/STAR	RRID:SCR_015899
ToppGene	http://toppgene.cchmc.org/	RRID:SCR_005726